Observability of Moisture Transport Divergence in Arctic Atmospheric Rivers by Dropsondes

Henning Dorff[1,2], Heike Konow[3,1], Vera Schemann[4], and Felix Ament[1,3]

[1]University of Hamburg, Hamburg, Germany
[2]International Max Planck Research School on Earth System Modelling, Max Planck Institute for Meteorology, Hamburg, Germany
[3]Max Planck Institute for Meteorology, Hamburg, Germany
[4]University of Cologne, Cologne, Germany

Correspondence: henning.dorff@uni-hamburg.de

Abstract. This study emulates dropsondes to elucidate how adequately sporadic airborne sondes represent divergence ~~(convergence)~~ of moisture transport in arctic Atmospheric Rivers (ARs). The convergence of vertically integrated moisture transport (IVT) plays a crucial role as it favours precipitation that significantly affects arctic sea ice properties. Long range research aircraft can transect ARs and ~~dropsondes~~ drop sondes to determine their IVT divergence. ~~However, a limited number of sondes may deteriorate the representation of~~ In order to assess the representativeness of future sonde-based IVT ~~variability and divergence . We~~ divergence in arctic ARs, we disentangle errors arising from undersampling by discrete soundings and from the flight duration~~in order to assess the representativeness of future sonde-based IVT divergence in arctic ARs~~.

Our synthetic study uses CARRA reanalyses to set up an idealised scenario for airborne AR observations. For nine arctic spring ARs, we mimic flights transecting each AR in CARRA and emulate sonde-based IVT representation by picking single vertical profiles. The emulation quantifies IVT divergence observability by two approaches. First, sonde-based IVT and its divergence are compared to the continuous IVT interpolated onto the flight cross-section. The comparison specifies uncertainties of discrete sonde-based IVT variability and divergence. Second, we determine how temporal AR evolution affects IVT divergence values by contrasting time-propagating sonde-based values with the divergence based on instantaneous snapshots.

For our arctic AR cross-sections, we find that ~~moisture transport variability contributes~~ coherent wind and moisture variability contribute by less than 10 % to ~~its lateral mean, while wind and moisture variability individually are higher~~the total transport. Both quantities ~~can be uncorrelated and do not consistently exhibit a coherent pattern~~are uncorrelated to a great extent. Moisture turns out as the more ~~varying~~ variable quantity. We show that sounding spacing greater than 100 km results in errors greater than 10 % of the total IVT along AR cross-sections. For IVT divergence, the arctic ~~ARs exhibit similar gradients~~ ARs exhibit similar differences in moisture advection and mass convergence across the embedded front as mid-latitude ARs, but we identify moisture advection being dominant. ~~We overall~~ Overall, we confirm their observability with an uncertainty ~~lower than~~ of up to 25 % ~~by~~ using a sequence of at least seven sondes per cross-section. Rather than sonde undersampling, it is the temporal AR evolution over the flight duration that leads to higher deviations in divergence components. Dedicated planning of sonde-based IVT divergence purposes should not only involve sonde positioning but rather pursue optimizing the

flight duration. Our benchmarks quantify sonde-based uncertainties as a prerequisite to be used for future airborne moisture budget closure in arctic ARs.

1 Introduction

~~Narrow~~ Atmospheric Rivers (ARs), which are elongated ($>$ 2000 km in length) but narrow ($<$ 1000 km in width) water vapour rich corridors ~~, ARs, occassionally flood~~ with high moisture transport, occasionally enter the Arctic. ~~In the polar regions, they account for~~ Their occurrence accounts for roughly 70 % of poleward moisture transport (Nash et al., 2018)~~with significant impacts (Gorodetskaya et al., 2014~~. The presence of ARs can induce significant Arctic warming (e.g. Neff et al., 2014) causing substantial sea-ice retreat (Woods and Caballero, 2016) as well as Greenland ice sheet melt (Mattingly et al., 2018; Neff, 2018). ~~Along the pathways of ARs, the moist and warm air masses undergo transformations that imply phase transitions, surface interaction or trigger significant precipitation (Lavers et al., 2016; Vázquez et al., 2018; You et al., 2022). The impacts range up to significant warming causing sea- and Greenland ice retreat (Gimeno et al., 2014; Woods and Caballero, 2016 ; Mattingly et al., 2018).~~ In addition to near-surface heat fluxes (Woods and Caballero, 2016; You et al., 2022), the melting arises from AR-induced precipitation (Mattingly et al., 2018; Viceto et al., 2022). Lauer et al. (2023b) identified ARs as one of the main contributors to overall arctic precipitation. The moisture needed for this is mainly extracted more southern, with the North Atlantic being a dominant moisture uptake zone (Vázquez et al., 2018). In an interplay with poleward moving cyclones and warm conveyor belts (e.g. Dacre et al., 2019), the AR air masses can propagate meridionally towards the Arctic ocean and reach the sea-ice (Papritz et al., 2021), shaping the regional moisture patterns (Nygård et al., 2020). Along the long-distance displacement, the AR embedded moist and warm air masses are subject to substantial air mass transformation (You et al., 2022) . Komatsu et al. (2018) discovered an amplification of air mass transformation after the ARs overpass the sea-ice edge.

To illuminate moisture transformation processes ~~and surface interactions (e.g. Papritz et al., 2021; You et al., 2022) occuring~~ occurring in arctic ARs, ~~we have to analyse the~~ it is crucial to grasp characteristics of the moisture transport, i.e. the ~~vertical Integrated Water Vapour Transport (IVT). The moisture budget links the evolution~~ vertically IVT. Seager and Henderson (2013) point out that the divergence of IVT links the local temporal evolution of moisture amount to the efficiency of precipitation induction. In order to derive IVT divergence, the spatial variability of ~~ARs and their precipitation efficiency by the divergence of IVT (Seager and Henderson, 2013). While the~~ in ARs needs to be resolved. Guan and Waliser (2015) considered global ECMWF Interim reanalysis (ERA-Interim, Dee et al., 2011) to specify strong moisture transport gradients that exist along AR cross-sections, perpendicular to the major IVT ~~variability and the contribution of~~ orientation. Along such lateral cross-sections through the AR center, a bell-shaped IVT ~~divergence to the moisture budget are widely assessed over the mid latitudes~~ distribution, having the strongest moisture transport in the AR core, is widely seen from airborne observations in mid-latitude ARs (e.g. ~~Guan et al., 2020; Tan et al., 2021), we lack an understanding of their magnitudes explicitly in~~ Ralph et al., 2017; Demirdjian et al., 2020). Using ERA5, Cobb et al. (2021b) confirm this heterogeneous spatial variability of IVT for mid-latitude ARs. For arctic AR conditions with weaker moisture transport than in the mid-latitudes, we still lack quantitative knowledge of predominant IVT variability and how this reflects to IVT divergence.

High-resolution observations of IVT variability to derive its divergence in ARs are missing for the Arctic. ~~Reanalysis data have been established a manifold understanding of global IVT variability in ARs (e. g. Guan and Waliser, 2015). Yet, such studies mostly stem of coarser grid reanalyses such as ERA-Interim and MERRA-2 (e.g. Guan and Waliser, 2017). Only recent studies include higher resolution reanalyses such as ERA5 which achieve more accurate AR-IVT representation (Cobb et al., 2021b) . High-resolution observations so far mainly exists for mid-latitude events that exhibit more intense moisture transport~~ One reason is the remote and sporadic occurrence of arctic ARs over the ocean basins. Furthermore, the observation of moisture transport requires simultaneous measurements of winds and moisture for the entire troposphere. Radiosondes allow detailed insights of moisture transport profiles of arctic ARs at individual locations (e.g. Viceto et al., 2022), but their observation network in the Arctic is too sparse to obtain the divergence in single ARs (Dufour et al., 2016). Similarly, dropsondes released from research aircraft can provide vertical profiles of relative humidity and wind speed with an accuracy of 1 % and 0.1 m/s, respectively (e.g~~Norris et al., 2020; Cobb et al., 2022)but, in turn, lack for the Arctic~~. George et al., 2021; Konow et al., 2021). The simultaneous measurements allow to derive moisture transport profiles and IVT. According to Zheng et al. (2021), dropsondes over ocean fill a data gap left by spaceborne remote sensing or ground-based observations. To derive the IVT divergence in ARs, it is necessary to release the sondes at close spacing but over horizontally extended areas above the AR which can only be achieved by long-range research aircraft (Neiman et al., 2014).

~~Still, the observation of arctic AR-~~The overall goal of this study is to assess the observability of moisture transport divergence in arctic ARs by dropsondes in order to facilitate dedicated research flight campaigns and measurement strategies, as e.g. proposed by Wendisch et al. (2021). This assessment comprises the role of sounding frequency, the influence of correlated moisture and wind fields on moisture transport, the ability of dropsondes to reproduce IVT ~~is challenging.One reason is the remote and sporadic occurence of arctic ARs over the ocean basins. Moreover, the quantification of AR moisture budget components, such as the divergence of moisture transport, requires sufficiently large horizontal corridors to be observed. ARs generally exhibit strong moisture transport gradients along their cross-section (~~divergence in arctic ARs and the impact of extended flight duration. The following paragraphs set these aspects into context with recent findings based on mid-latitude ARs and unravel four research gaps for arctic ARs, summarised as guiding science questions.

Deteriorations in the airborne representation of AR moisture transport variability can result from a limited number of sondes if the sounding spacing becomes too coarse to reflect the spatial variability of IVT. The sondes may misinterpret IVT divergence. For mid-latitude ARs, Guan et al. (2018) compared sonde-based Total Integrated Water Vapour Transport ($TIVT$) , being the integral of IVT along an AR cross-section, with reanalysis-based $TIVT$ and found an agreement up to 3 % for airborne results based on a mean sounding spacing of 80 km. Contrasting the airborne $TIVT$ in two separate AR cross-section legs can serve as an initial estimate of IVT divergence in between both legs. However, Ralph et al. (2017) found considerable sensitivity of sonde-based $TIVT$ to sonde spacing. Enlarging the initial spacing between the sondes by reducing the number of included sondes, they found a mean deviation of at least 5 % for $TIVT$ when doubling the spacing. Since given sensitivity studies refer purely to mid-latitude cases where we do expect higher $TIVT$ (Guan et al., 2018), it remains as open question: *What is the maximum distance between sondes to determine the total moisture transport in arctic AR cross-sections (Q1)?*

When assessing spatial IVT variability in arctic ARs, it becomes crucial how moisture and wind fields coincide in the

AR cross-section or whether they contribute independently to the IVT variability. For instance, in a polar AR case study, Terpstra et al. (2021) identified incoherent patterns of moisture and wind that form the moisture transport patterns but are less aligned than in mid-latitude ARs. The disentanglement of both quantities facilitates flight strategies in the observation of moisture transport divergence in arctic ARs. If the moisture transport variability (and divergence) were e.g. ~~Ralph et al., 2017; Demirdjian et al., 2020)~~mainly controlled by the moisture field, more investment should be spent on the airborne representation of AR moisture by supplementary measurements. For this reason, it is important to determine whether moisture and wind are aligned in AR cross-sections and to ascertain: *How correlated are moisture and winds in arctic ARs and do coherent patterns contribute significantly to IVT (Q2)?*

Knowing the spatial structure of IVT is an essential prerequisite for flight planning and reveals insights into the moisture transport divergence pattern in arctic AR cross-sections. Since ARs ~~mainly occur in conjuction~~ primarily occur in conjunction with a cold front, different ~~dynamical and thermodynamical~~ dynamic and thermodynamic processes act on the moisture transport and its divergence ~~along the frontal cross-section (Guan et al., 2020, Cobb et al., 2021a). Other than that,~~ across the embedded front (Cobb et al., 2021a). For mid-latitude ARs, Cobb et al. (2021a) found significant differences of vertical moisture and wind domains for different sectors across the front which transfer to frontal gradients in divergence characteristics (Guan et al., 2020). Using reanalysis data, Guan et al. (2020) specified lateral differences of moisture ~~transport observation has to rely on simultaneous measurements of winds and moisture . Dropsondes can measure the vertical profiles of both quantities and thus the moisture transport so that they close a data gap remaining from remote sensing and from spaceborne or ground-based observations in general (Zheng et al., 2021). From long-range research aircraft, sonde releases enable the observation of~~ transport divergence across centers of ARs. In the AR center with maximum IVT, they identified the dynamical convergence of moisture as the most prominent component regulating moisture amount and precipitation. The Arctic is more affected by exit regions of ARs rather than over-passed by AR centres and exhibits weaker IVT from ARs compared to the mid-latitudes (Guan and Waliser, 2019). ARs here commonly start dissipating and terminating (Guan et al., 2023). For such conditions, we lack knowledge of predominant IVT divergence~~in extended sectors of ARs. First airborne studies~~. Thus, we examine: *How can the divergence of moisture transport be characterised along cross-sections of arctic ARs (Q3)?*

Norris et al. (2020) conducted airborne studies to determine IVT divergence in mid-latitude ARs ~~(e.g. Norris et al., 2020) and begin complementing large reanalysis-based statistics of AR moisture budget components (Guan et al., 2020). However, a limited number of dropsondesmay deteriorate the~~ from dropsondes. Such research flights allow to interpret the discrepancies that Guan et al. (2020) found between reanalyses in representing IVT ~~representation and consequently the divergence values. Accordingly, studies assess the impact of sounding frequency on AR~~ divergence in ARs. In contrast, Norris et al. (2020) point to the large variability of IVT ~~variability (e. g. Ralph et al., 2017; Guan et al., 2018), but so far purely for mid-latitude ARs. Besides~~ divergence at spatial scales of 50 km which has implications for sonde-based ~~undersampling, we hypothesize that~~ results. For arctic AR conditions, we lack equivalent estimates. Moreover, besides sonde-based under-sampling of IVT variability and divergence, we hypothesise that airborne results are also impaired by a time component. Over the flight duration required to enclose an AR corridor, the temporal evolution of the AR (its life cycle and spatial displacement) can affect the ~~AR evolution over the flight duration enclosing the AR corridorcan also affect the results non-negligibly. Before sondes infer~~

sonde-based results significantly. Before dropsondes are used to interpret the actual IVT divergence in arctic ~~ARs, we~~ ARs , we have to disentangle sonde-based errors that arise from undersampling by discrete sounding and from non-instantaneous sampling over the flight duration. ~~Therefore, we examine how moisture transport variability is composed in arctic ARs close to the sea ice~~ We quantify: *To what extent do non-instantaneous sondes reproduce IVT divergence in the light of the AR evolution during flight (Q4)?*

To pursue Q1-Q4, we focus on ARs occurring over the Arctic ocean (i.e. Fram Strait and Greenland Sea) ~~. Our study monitors AR moisture transport as seen from long-range research aircraft to tackle how such aircraft infer arctic AR moisture transport variability by adressing the questions:~~

- ~~(Q1) What is the maximum distance between sondes to determine the total moisture transport through AR corridors?~~
- ~~(Q2) How correlated are moisture and winds in arctic ARs and do coherent patterns contribute significantly to IVT?~~

~~As a prerequisite to close the moisture budget for arctic AR cross-sections, we assess the observability of moisture transport (IVT) divergence by dropsondes and quantify uncertainties in its representativeness. Our divergence assessment comprises:~~

- ~~(Q3) How does divergence of moisture transport characterise along the cross-section of arctic ARs ?~~
- ~~(Q4) To what extent can discrete and non-instantaneous sondes reproduce IVT divergence in the light of the AR evolution during flight?~~

~~To pursue Q1-Q4, we~~ in the vicinity of the sea-ice edge due to the above-mentioned AR impacts on the sea-ice. We constrain on ARs during spring, when maximum sea-ice extent starts melting. We look at arctic ARs ~~, that we pre-identified in ERA5 and investigate them~~ within the novel C3S Arctic Regional Reanalysis (CARRA). ~~The high spatial resolution of CARRA illuminates kilometer-scale moisture transport variability inside arctic ARs and forms our idealized background reality. In CARRA~~Introducing a flight strategy to analyse moisture transport divergence in arctic AR corridors, we consider ~~nine~~ arctic AR events along synthetic ~~flights transecting and enclosing~~ flight tracks that transect an AR corridor. We emulate synthetic dropsondes along the tracks by depicting single vertical profiles. ~~Our~~ This study compares actual IVT variability and divergence along the flight tracks with the emulated sonde-based ~~IVT representation . This synthetic comparison estimates the observability of arctic~~ representation of IVT in order to assess how adequately such airborne perspectives reproduce predominant AR-IVT characteristics. In a nutshell, our synthetic assessment provides benchmarks of sonde-based uncertainties in their representation of IVT divergence ~~from sondes~~in arctic ARs to facilitate future mission planning.

~~Section ?? presents our considered AR events in CARRA. Section ??~~ The remainder of the manuscript is structured as follows: After introducing our AR cases, Section 2 describes the methods emulating dedicated flight ~~pattern and the~~ patterns and synthetic soundings, and how we derive moisture transport divergence. For this framework, Section 3 deals with the IVT variability. This entails total moisture transport ~~in arctic ARs and their~~ and the IVT variability along cross-sections in arctic ARs , their sonde-based representation (Q1) and the coherence of moisture and winds (Q2). Section 4 specifies the moisture transport divergence in arctic ARs (Q3) and compares its continuous representation to that by ~~synthetic~~ sporadic sondes. Section 5 quantifies airborne deviations arising from AR evolution over flight duration ~~which is mostly idealized~~ that is mostly idealised

as stationary (Q4). ~~Our assessment provides benchmarks of uncertainties in the sonde-based IVT divergence for arctic AR and facilitates flight mission planning.~~

2 ~~Arctic AR moisture transport data~~

1.1 ~~Dropsondes on long-range research aircraft~~

~~This study relies on the flight performance of state-of-the-art long-range research aircraft. We exemplarily refer to the High Altitude and LO~~
~~, equipped with a remote sensing configuration described in more detail in Stevens et al. (2019) and Konow et al. (2021). A similar aircraft examines pacific ARs (Cobb et al., 2022). Both aircraft allow along-track observations during flight at common cruising levels above 10 km and a ground speed of around 250 m/s.~~

2 Airborne derivation of moisture transport divergence in arctic ARs

The central quantity of our study is the Integrated Water Vapour Transport (IVT) that represents the AR intensity as:

$$IVT = -\frac{1}{g} \cdot \int_{p_{\mathrm{sfc}}}^{p_{\mathrm{top}}} q\mathbf{V}\, dp \tag{1}$$

where $\mathbf{V}$ is the horizontal wind vector and q the specific humidity. The divergence of IVT represents a key component contributing to the overall atmospheric moisture budget. Following Seager and Henderson (2013), the vertically integrated moisture budget components consist of:

$$\underbrace{\frac{\delta IWV}{\delta t}}_{\text{local change in Integrated Water Vapour}} = \underbrace{E}_{\text{Evaporation}} - \underbrace{P}_{\text{Precipitation}} - \underbrace{\nabla IVT}_{\text{Divergence of Integrated Water Vapour Transport}}, \tag{2}$$

with all components in kilogram per metre squared per second. Precipitation and evaporation refer to surface values, while the integrated water vapour IWV and IVT (Eq. 1) represent the vertically integrated quantities of moisture and moisture transport. Note that Eq. 2 neglects the moisture flux through a tilted bottom pressure surface that is included in Seager and Henderson (2013)
.

~~Such aircraft release GPS-dropsondes. During their fall,~~ Given the relevance of IVT to the ~~sondes take various measurements, e.g. relative humidity and wind speed with an accuracy of 1 % and 0.1 m/s, respectively (George et al., 2021; Konow et al. , 2021) . The simultaneous measurements allow to derive the moisture transport~~ AR moisture budget, this feasibility study targets the overall observability of IVT and its divergence ~~inside Arctic ARs . We refer to such a sonde principle, but we neglect the explicit measurement uncertainties for both quantities. Instead, we target the overall representativeness of airborne~~ (∇IVT) in arctic ARs by airborne sondes in a synthetic way. For this purpose, this section introduces the reanalysis framework we use to investigate a presented selection of arctic ARs. In addition, our airborne flight strategy to derive ∇IVT in arctic ARs

Table 1. Specifications of used reanalyses for AR analysis

Reanalysis Dataset	Horizontal Resolution	Vertical resolution up to 10 km (~~250~~≈ 250 hPa)	Time resolution
ERA5	0.25 x 0.25 deg	21 levels	hourly
CARRA	2.5 x 2.5 km	15 levels	~~(forecast hourly)~~ hourly

is specified and how we emulate the synthetic sondes in the reanalyses. Lastly, we describe the sonde-based ~~IVT. For arctic conditions, we synthetically assess sonde-based uncertainties in lateral moisture transport variability, its maximum intensity and position and how the uncertainties affect airborne IVT divergencecalculations~~derivation of ∇IVT and how we categorise different sectors across the AR front to examine the divergence.

190

2.1 Reanalysis ~~data~~framework

This ~~observability study relies on~~ study investigates arctic ARs in a reanalysis framework (Tab. 1). ~~The~~ We use ECMWF Reanalysis v5 (ERA5) (Hersbach et al., 2020) ~~identifies our ARs of interest. Against~~ to identify the AR events of our interest. ERA5 outperforms other global reanalyses ~~, ERA5 outperforms~~ with respect to AR characteristics (Graham et al., 2019; Cobb
195 et al., 2021b). ~~Recent~~ Thus, recent studies consider ERA5 to investigate AR conditions ~~explicitly~~ specifically in the Arctic (e.g. Fearon et al., 2021; Zhang et al., 2022). At the Fram Strait and Greenland Sea, the lat-lon grid from ERA5 yields approximately 30 km distances. ~~For~~ Given the flight performance ~~(Sect. 2.1), sounding resolutions of 30 km~~ of long-range research aircraft (see Stevens et al., 2019), the spacing of airborne soundings in such a resolution would require releases every 2 minutes, which are more frequent than conducted in recent campaigns (e.g. Ralph et al., 2017). Still, Skamarock et al. (2014)
200 emphasise that the effective resolution of processes in simulations is much greater than the model grid spacing. ~~This is higher than commonly conducted sounding frequencies.~~ However, ~~to cover undersampled variability between the sondes even better, we~~ if our study aims to assess the sub-grid scale variability of moisture transport between sonde releases from reanalyses, the effective resolution should be of the order of ~ 10 km rather than of ~ 100 km.

Therefore, we further include the C3S Arctic Regional Reanalysis (CARRA)~~, accessible by Schyberg et al. (2021), having~~ ,
205 CARRA has a 2.5 km horizontal resolution over the entire domain and is accessible by Schyberg et al. (2021). Driven by lateral boundary conditions from ERA5, CARRA includes more observations and hourly forecasts by the HARMONIE-AROME model (Bengtsson et al., 2017). Køltzow et al. (2022) verified the improved representation ~~in~~ of arctic surface-near meteorological conditions ~~. Both pressure-level~~ in CARRA, with decorrelation lengths of wind speed in better agreement to reference observations than ERA5.

210 Both reanalyses are provided on pressure levels by the Copernicus Climate Data Store (CDS). While ERA5 contains IVT as output, we calculate IVT in CARRA by the trapezoidal integral of moisture transport along the pressure levels (Tab. 1). In the

following, we declare the high spatial resolution representation in CARRA as our idealised background reality of AR features.

2.2 ~~Selected~~ Selection of Atmospheric River cases

~~Our study comprises ARs from nine spring days between 2011 and 2020. Figure 1 presents these ARs extending over the North Atlantic and Arctic Ocean. Accordingly, we are interested in ARs causing airmasses~~ The transformation of arctic air masses over changing surface types (open ocean and sea-ice) along large-scale meridional circulations is part of current research and investigated by research aircraft over the Arctic ocean (Wendisch et al., 2021). For this reason, our study selects ARs causing air masses to overshoot the sea ice edge in ~~the Arctic ocean. As a valid AR detector we use~~ this region. The principle identification of arctic AR events is based on the IVT ~~that represents AR strength as:~~

$$IVT = -\frac{1}{g} \cdot \int_{p_{\mathrm{sfc}}}^{p_{\mathrm{top}}} q\mathbf{V}\, dp$$

~~where $\mathbf{V}$ is the horizontal wind vector and q the specific humidity. We use~~ IVT-based AR detection ~~by Guan (2022) to select our arctic ARsfrom spring season~~catalogue by Guan (2022) applied to ERA5 (Lauer et al., 2023a). Among these ARs, we focus on the spring season, when maximum sea-ice extent in the Arctic ocean starts to break-up and reacts very prone to the intrusion of warm and moist air (Rostosky and Spreen, 2023). We restrict to conditions and events only from last decade, as the arctic climate has witnessed rapid and intense changes over the last decades (Wendisch et al., 2023). Our AR pathways originate from the North Atlantic and Barents Sea that Papritz et al. (2021) spot as dominant regions for arctic moisture intrusions. The selection constrains on ARs whose lateral width is purely situated over open ocean or sea-ice. This ensures that we do not encounter orographic induced effects on ∇IVT which are out of the scope of this study. Moreover, airborne sonde releases over land are more complicated to be conducted. Given the criteria above, we selected ARs from nine spring days between 2011 and 2020, presented in Fig. 1.

~~The selected ARs take typical arctic pathways (Fig. 1).Usually, arctic ARs evolve on the eastern flank of~~ In the synoptic composition of a Greenland trough, low-pressure systems ~~forcing~~ force large-scale meridional transport ~~representing a common synoptic composition (Papritz and Dunn-Sigouin, 2020). Blocking situations can favor even more~~ where ARs can commonly evolve on the eastern cyclone flank and reach into the Arctic (Papritz and Dunn-Sigouin, 2020). Similarly, blocking situations over Eurasia can favor meridional circulation. ~~Some of the~~ For our nine ARs (Fig. 1), we confirm a large case-to-case variability regarding the synoptic situation. While some ARs (AR2, AR3, AR4, AR9) have evolved along the eastern flank of large-scale troughs over Greenland, AR5 and AR6 are more steered by blocking high pressure over the Barents Sea. AR1 and AR7 are, in turn, reinforced by a mesoscale cyclone situated over the Fram Strait and reach very close into the cyclone center.

The synoptic compositions lead to AR dispersions over the North Atlantic and Arctic Ocean (Fig. 1), which correspond to the typical arctic moisture transport pathways identified in Papritz et al. (2021). Some ARs exhibit straight meridional moisture transport north of Iceland and approach or exceed Svalbard (AR1, AR2, AR3 in Fig. 1). AR4 and AR7 show more elongated filaments along the Norwegian coast but still reach far north. We ~~select eight independent~~ consider eight independent AR

~~IVT contours of investigated AR events from ERA5. Red lines represent the zig-zag flight pattern to investigate the moisture budget in AR corridors. Grey lines indicate surface isobars, while brown (orange) contour lines specify sea ice cover thresholds given in %. The arrows depict the magnitude and orientation of IVT. Background maps were made with Natural Earth.~~

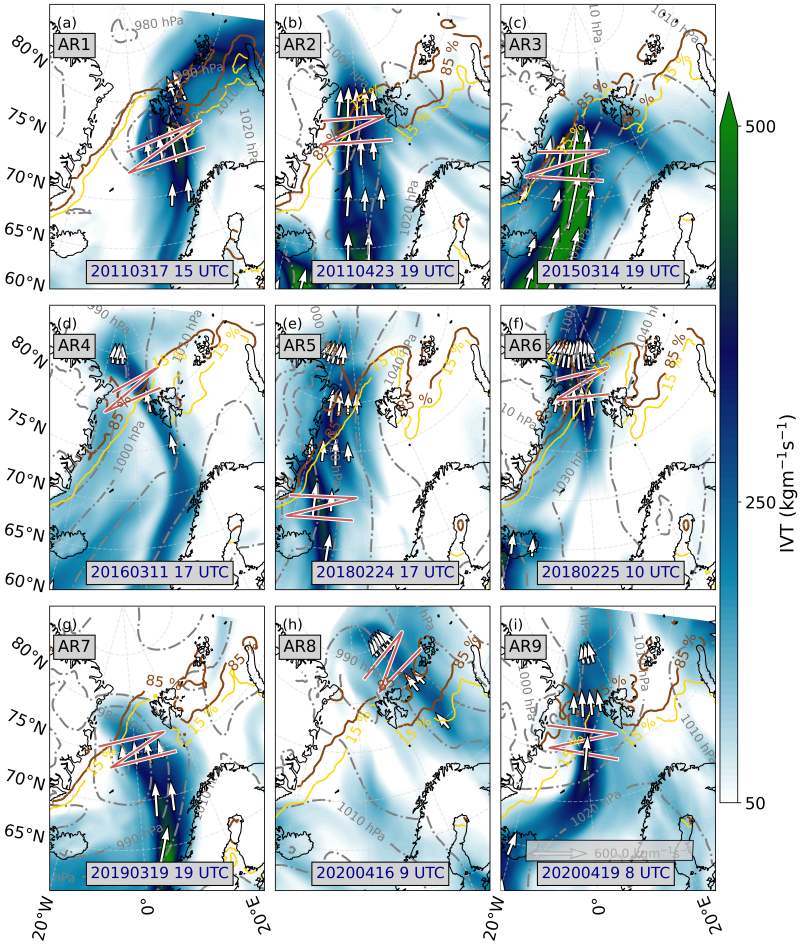

Figure 1. IVT contours of investigated AR events from ERA5. Grey lines indicate surface isobars, while brown (orange) contour lines specify sea ice cover thresholds given in %. The arrows depict the magnitude and orientation of IVT. Red lines represent the zig-zag flight patterns to investigate the moisture budget in AR corridors. Background maps were made with Natural Earth.

events wherein AR5 is also considered for the consecutive day (AR6). At this stage, the centre of AR6 reaches close to the North Pole. ~~Another event~~ AR8 originates from Siberia ~~(AR8) that~~that, according to Komatsu et al. (2018), represents another significant roadway for arctic moisture intrusions ~~(Komatsu et al., 2018)~~favoring ARs. The last events in 2020 (AR8, AR9) are accompanied by a warm air intrusion period observed by the Multidisciplinary drifting Observatory for the Study of Arctic Climate (MOSAiC) expedition (Shupe et al., 2022), studied in Kirbus et al. (2023).

~~Since our analysis is restricted to a small set of ARs, we put them into perspective of spring climatology . Picking the events~~

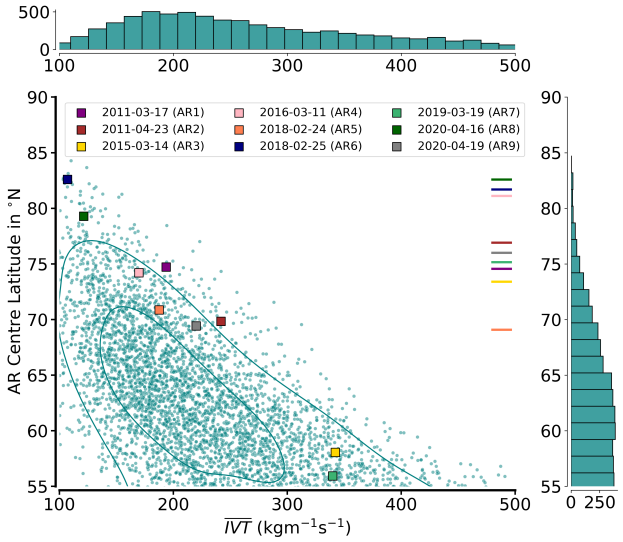

gl[t!]

Figure 2. Comparison of selected AR events to long-term statistics (1979–2019) regarding mean IVT and AR centre latitude at given reanalysis time step (ERA-Interim) based on the AR catalogue ~~(Guan, 2022)~~of Guan (2022). Isolines represent ~~25~~ 25th and ~~75~~ 75th percentiles of the kernel density estimate. Coloured lines on the right indicate the centre of the respective flight pattern.

~~from the AR~~ A caveat of our selection for making general statements about IVT variability in arctic ARs is the small sample size (nine AR events). Therefore, we place our events in the climatology for arctic ARs in spring. Using the entirety of spring ARs along the Atlantic pathway from the catalogue of Guan (2022), ~~Figure 2 compares~~ we compare the latitude of ~~their~~ the AR centres and mean IVT of our ARs with the long-term distribution (1979–2019) for spring ARs ~~along the Atlantic pathway. The distribution indicates that ARs centred further north are aligned with less intense~~ (Fig. 2). The climatological distribution in Fig. 2 indicates the decrease of mean IVT ~~. Our selected ARs characterise a higher intensity compared to the long-term mean. Most events are centred above~~ with meridional location of the AR centre. Further towards the Arctic, ARs become weaker and when centered north of 65°N~~with~~ , the mean IVT remains below 300 kg m^{-1} s^{-1} ~~which is also not exceeded in the climatology.~~ . This is also the case for our AR events but they, in turn, are characterized by a higher intensity relative to the long-term mean (Fig. 2). Only AR3 and AR7 are centred below 60°N, aligned with mean IVT values around 350 kg m^{-1}s^{-1}. ~~Despite~~ However, despite their southern centre, they reach far north with $IVT > 250$ kg m^{-1}s^{-1} inside the Fram Strait (Fig. 1), so that we declare them as arctic ARs. ~~The flights transecting AR corridors are located in vicinity of the arctic sea ice edge and mainly north of the AR centre (~~We conclude from Fig. 2 ~~).~~

3 ~~Airborne strategy for AR moisture transport divergence~~

The moisture transport divergence is one key component contributing to the overall atmospheric moisture budget. In a vertically integrated perspective, the moisture budget components consist of:

$$\underbrace{\frac{\delta IWV}{\delta t}}_{\text{local change in Integrated Water Vapour}} = \underbrace{E}_{\text{Evaporation}} - \underbrace{P}_{\text{Precipitation}} - \underbrace{\nabla IVT}_{\text{Divergence of Integrated Water Vapour Transport}} ,$$

with all components in kilogram per metre squared per second. Seager and Henderson (2013) include another term in Eq. 2, being the moisture flux through a tilted bottom pressure surface, but this is less relevant here. Precipitation and evaporation refer to surface values, while the integrated water vapour IWV and integrated water vapour transport IVT (Eq. 1) represent the vertically integrated quantities. We calculate CARRA-IVT as the trapezoidal integral along the pressure levels (Tab. 1). The following section specifies our airborne strategy to derive ∇IVT in arctic ARs therefrom and the sonde emulation.

2.1 Flight pattern and emulating observations

The main perspective is that our cases represent the stronger AR events occurring in the Arctic.

2.1 Flight pattern and emulated observations

Having introduced our AR cases, this subsection returns to the perspective of the airborne observability of ∇IVT inside arctic ARs. To mimic real observations as a prerequisite for upcoming campaigns, this section emulates sophisticated We describe the emulation of real observations by mimicking dedicated flight patterns and creates synthetic soundingsalong the flightscreating synthetic soundings.

2.1.1 Zig-zag flight tracks observing AR corridors

The For the airborne derivation of moisture transport divergencerequires sophisticated flight patterns well sampling a specific AR corridor, flight patterns have to well sample specific corridors of the AR. In general, flight tracks enclosing corridors, e.g. circles, allow divergence calculations best and are frequently applied for closure purposes (Bony and Stevens, 2019)such purposes (e.g. Bony and Stevens, 2019). However, ARs exhibit cross-frontal inhomogenities (Cobb et al., 2022) that heterogeneity in moisture and wind fields (Cobb et al., 2021a) that would smooth out in single circles. The Instead, the high lateral variability in AR AR moisture transport characteristics requires stacked or long flight legs across the AR front to better capture divergence heterogeneity. Two parallel cross-sections can be connected via an internal flight leg resulting in a zig-zag patterns with long legs crossing the AR front to capture the heterogenity more sufficiently. Figure 3 sketches how the latter pattern is conceptionally applied in order to close the moisture budget in ARs. flight pattern (Fig. 3). The zig-zag pattern observes AR corridors , i.e. box sections along corridors of the AR across its transport direction. Diagonal internal legs assess precipitation rate, evaporation or water load inside. The boundary The boundary cross-section legs perpendicular to the major flow quantify the corridor in- and outflow, i.e. in- and outgoing IVT for over the entire lateral AR extension . These legs and enable simplified divergence calculations. Top (a) and side (b) view on envisioned zig-zag flight pattern to derive the moisture budget

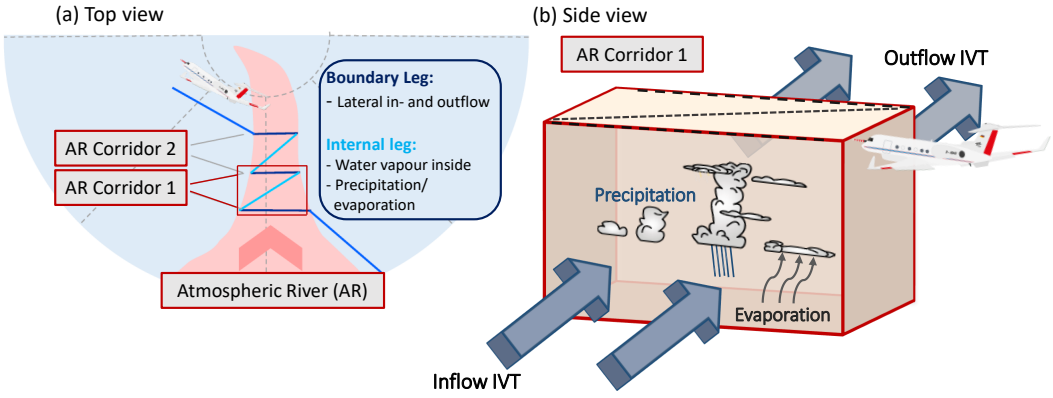

Figure 3. Top (a) and side (b) view on envisioned zig-zag flight pattern to derive the moisture budget components inside AR corridors.

components inside AR corridors. We select AR Note that the diagonal internal legs can assess precipitation rate, evaporation or water load inside the AR corridor so that this pattern additionally allows to quantify the remaining moisture budget components.

According to Fig. 1, we place such zig-zag flight patterns over AR corridors at the sea ice edgeto place the zig-zag flight pattern in (Fig. 1). The corridor boundary legs orientate orthogonally . The cross-section legs orientate orthogonal to the major IVT direction . The zig-zag patterns extend in such a way that they cover entire AR cross-sections, meaning the prefrontal warm sector, the AR core with highest IVT and the postfrontal AR cold sector. We fly IVT direction and extend such that they cross the entire AR as long as the legs remain over open ocean and sea ice but and disregard land. The tracks mimic idealised flight performances. The aircraftlocation refers to 1As depicted in Fig. 2, the flights transecting the AR corridors close to the sea-ice are mainly located north of AR centres.

For the airborne representation, we mimic the flight performance of state-of-the-art long-range research aircraft. We refer to the HALO, equipped with dropsondes and a remote sensing configuration (Stevens et al., 2019; Konow et al., 2021); a similar aircraft like the one examining pacific ARs, specified in Cobb et al. (2022). Both aircraft allow along-track observations during flight at common cruising levels above 10 Hz resolution which is a common resolution of remote sensing products, such as the HAMP dataset comprising radiometer and radar (Mech et al., 2014; Konow et al., 2019). We assume a km and a ground speed of around 250 m/s. Accordingly, we idealize flights with a constant ground speed of 250 m s^{-1} but neglect the duration for turns . We and choose a constant flight altitude of 10 km. From this, 000we represent the aircraft location in a 1 m.

2.1.2 Synthetic observations

Using thisidealised performance, the Hz resolution, in line with the operational resolution of common airborne remote-sensing products (e.g. Mech et al., 2014; Konow et al., 2019) that can support dropsonde data. The zig-zag patterns(, shown in Fig. 1) , require roughly 2–3 h to be completedflown, and up to 1 h for the single AR cross-sections(not shown). Up .

Using this idealised flight performance, up to three reanalysis timesteps time steps represent atmospheric conditions during our patternthe flights. We upsample the reanalysis datasets data to minutely frequency by linear time interpolation. Meteorological

values along the flight are chosen For our 1 Hz representation of flight location, we depict the reanalysis values from the nearest minute and spatially interpolated interpolate them along the flight using harvesine distances. Although This representation of meteorological values and AR characteristics will from now on be referred to as "continuous AR representation". Admittedly, the upsampling leaves the model physics at intermediate timestepstime steps. However, we declare this the interpolation as a suitable airborne estimate of atmospheric conditions estimate of airborne atmospheric observations in dynamic systems like ARs, exhibiting ARs that are subject to significant spatial displacement.

2.1.2 Synthetic dropsondes

We synthetically refer to the measurement principle of dropsondes (Sect. 1). Along the continuous airborne AR representation , we place (Sect. 2.1.1), we depict profiles as synthetic soundings for which we neglect any vertical drift or fall time. We further neglect pure also neglect any measurement uncertainties. Mimicking such effects is Such effects are out of the scope of this studyalthough it may be crucial when evaluating real sonde profiles with model data. Instead, our . Our sondes observe exact IVT values at their release position. Accordingly, our assessment focusses we focus on the spatial representativeness of dropsondes and especially how their release frequency may affect the airborne understanding sporadic sonde-based IVT and evaluate the uncertainties in the lateral variability of moisture transportvariability and its , and how these uncertainties affect the airborne perspective on IVT divergence in arctic ARs. ARs.

2.2 Sonde-based divergence derivation

To determine derive ∇IVT in AR corridors from sondes, a simplified approximation relies on deriving the Total Integrated Water Vapour T of both cross-section legs in Fig. 3. Following Ralph et al. (2017), $TIVT$ of a cross-section is defined as:

$$TIVT = \int IVT\, dx, \tag{3}$$

representing the lateral integral of IVT divergence (over the flight distance x in a respective cross-section flight leg. Neglecting the moisture flux that exists apart from perpendicular to the flight track, we can approximate ∇IVT), the in an AR corridor by the difference of out- minus ingoing $TIVT$ of the cross-sections. However, this excludes any divergence of the flow perpendicular to the cross-section.

The Gaussian Theorem sets the moisture flux over the perimeter of a closed surface equal to its divergence. However, our flight pattern (Fig. 3) has open boundaries at the outer sides. Only if lateral flow can be neglected, we can obtain the divergence by subtracting the inflow in the entrance leg from the streamward outflow(Fig. 3). . Given this limitation, Lenschow et al. (2007) alternatively suggests the regression method. Under linear variations, a meteorological quantity Φ (e.g. wind speed) , being that is stationary in time , can be inferred as:

$$\Phi = \Phi_o + \frac{\delta\Phi}{\delta x} \cdot \Delta x + \frac{\delta\Phi}{\delta y} \cdot \Delta y, \tag{4}$$

with the area mean value Φ_o and Δx and Δy being zonal, meridional displacements from the area centre point. Using the values of Φ at sounding locations and minimising the least-squared errors in the linear regression fit of Eq. 4, we obtain a linear

estimate of zonal (x) and meridional (y) gradients, along with ~~the intercept for the line, providing the~~ the mean mesoscale value for Φ. Adding up both gradients, we calculate the divergence. Bony and Stevens (2019) and George et al. (2021) proved the feasibility of this method by comparing its divergence values with the Gaussian-based line integral over flown circles.

Having the mathematical expression, we ~~specify~~ view on the impact of IVT divergence~~with respect to the moisture budget. In case of evaporation E being negligible compared to the other terms of Eq. 2 (what approximately holds for the open Arctic Ocean), convergence of integrated moisture transport either causes precipitation or locally increases the amount of water vapour. Since convergence of moisture transport hence has two different impacts, ∇IVT~~. The divergence of moisture transport can be split ~~into two composits:~~ up into two components:

$$\nabla IVT = -\frac{1}{g \cdot \rho_w} \cdot \int_{p_{\mathrm{sfc}}}^{p_{\mathrm{top}}} \nabla\,(q\mathbf{V})\,dp = \underbrace{\frac{1}{g \cdot \rho_w} \cdot \int_{p_{\mathrm{sfc}}}^{p_{\mathrm{top}}} q\,(-\nabla \mathbf{V})\,dp}_{\text{dynamical mass convergence (CONV)}} + \underbrace{\frac{1}{g \cdot \rho_w} \cdot \int_{p_{\mathrm{sfc}}}^{p_{\mathrm{top}}} \mathbf{V}\,(-\nabla q)\,dp}_{\text{integral of horizontal moisture advection (ADV)}} \quad . \tag{5}$$

The first term represents the dynamical mass convergence being the product of the moisture mass and divergence. The mass convergence term can be related to vertical velocity via the continuity equation and itself is closely linked to precipitation (Wong et al., 2016; Norris et al., 2020). The second term represents the horizontal advection of moisture that ~~is~~ Guan et al. (2020) shows to be little correlated to precipitation formation~~(Guan et al., 2020).~~. Instead, it locally affects the amount of water vapour. To calculate ADV and $CONV$, we use the regression method. Finally, all terms in Eq. 5 are divided by the density of water ρ_w to provide ~~budget contributions in mm per day (mm d^{-1}).~~ their contributions to the moisture budget (Eq. 2) in mm d^{-1}.

2.3 Decomposition in ~~frontal~~ AR frontal sectors

Current research considering ~~observations along AR cross-sections~~ IVT divergence in ARs suggests to distinguish between different sectors ~~across the front the AR is embedded in . This separation results from the ARoccurence mostly within the vicinity of cold fronts where distinct processes~~ along the lateral AR cross-sections. Guan et al. (2020) highlight the cold-frontal structures that are commonly embedded in the AR, where different dynamics take place. ~~Using~~ Hence, Guan et al. (2020) separate IVT divergence calculations across the major AR axis and the AR embedded front. Similarly, using airborne observations of a large set of pacific AR cross-sections, Cobb et al. (2021a) classified different sectors ~~of~~ in ARs based on the ~~frontal position~~ position of the AR embedded cold front and IVT ~~. This comprises a warm sector being~~ shape. Both approaches distinguish between a pre-frontal (warm) sector, the AR core with highest IVT ~~(> 80 % of maximum IVT)~~ and the post-frontal ~~cold sector. Similarly, Guan et al. (2020) refer to their global AR catalogue and separate AR cross-sections for~~ (cold) sector behind the cold front. Since there exist significant frontal differences in moisture transport divergence between the sectors (Guan et al., 2020), a lot of variability is smoothed out when calculating IVT divergence ~~calculations across the major AR axis~~for entire cross-sections.

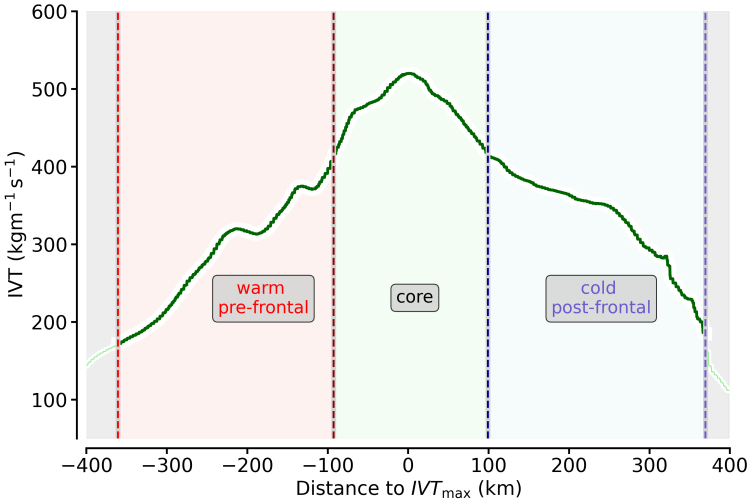

Figure 4. Frontal sector decomposition for an exemplary IVT cross-section (AR1) using the criteria described in Sect. 2.3. The colored shadings and text boxes indicate each frontal sector. The grey shading on the left represents moisture transport (i.e. IVT) that is not considered as AR because it is too weak.

~~Illustration of AR cross-section sectors and placed sondes in order to calculate the divergence for AR3. IVT contours refer to CARRA at the hour mid of the flight corridor. Background map is made with Natural Earth.~~ ~~We conduct such~~ Therefore, we conduct a similar sector-based decomposition of IVT divergence for our arctic AR events in CARRA. ~~Figure 5 illustrates the frontal sector decomposition for our most intense AR (AR3). Our decomposition aligns with the requirements given in~~ As in Guan et al. (2020) and Cobb et al. (2021a), our decomposition relies on the IVT characteristics along the cross-section, which we depict for an exemplary AR cross-section in Fig. 4. The central AR core represents the region of strongest IVT, which is more than 80 % of maximum IVT (IVT_{max}). East of the core we situate the pre-frontal sector and west the post-frontal sector. Yet, the outer edges of the frontal sectors are less trivial as ARs basically have no clear outer boundaries. To account for case-specific relative values, we assign both frontal edges where $IVT \leq 0.33 \cdot IVT_{max}$ (Fig. 4). As a secondary absolute threshold, we declare a moisture transport with $IVT \leq 100\,\mathrm{kg\,m^{-1}\,s^{-1}}$ as too weak to be assigned as AR. Both conditions form the outer edges of the AR where the pre- and post-frontal sectors end. Note that the latter threshold to define the AR edges follows the approach of Cobb et al. (2021a). However, we lower ~~the~~ their mid-latitude based IVT ~~-threshold defining AR edges from 250~~ threshold from 250 to $100\,\mathrm{kg\,m^{-1}\,s^{-1}}$. ~~This fits~~ By this, we refer to common polar moisture transport magnitudes ~~exceeding~~ that exceed the 95th percentile ~~used in the AR~~ of climatology and are declared as ARs in the detection of Guan and Waliser (2015). Otherwise, ~~as statistics in Fig. 2 indicate, we would~~ we would either exclude most ARs north of 70~~°N,~~°N or would shrink the AR cross-section so much that most transport is ignored~~. As shown~~, as the statistics in Fig. ~~5, three synthetic sondes calculate the~~ 2 indicate.

Applying the frontal classification to both cross-sections, we obtain three sectors. For the cross-sections of the AR, we locate the sondes so that six synthetic sondes (three each from the in- and outflow cross-section) span each frontal sector and calculate

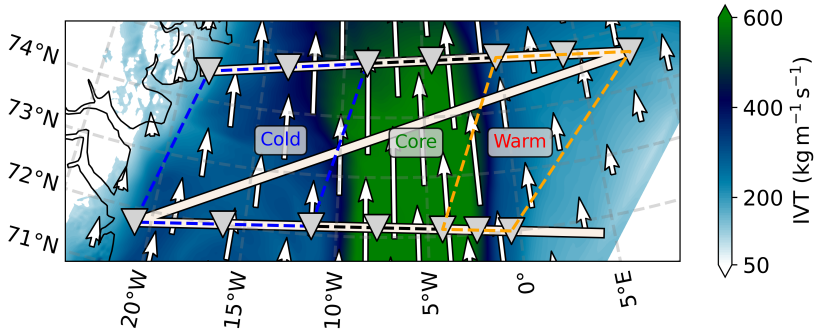

Figure 5. Illustration of AR cross-section sectors and placed sondes to calculate the divergence for AR3. IVT contours refer to CARRA at the hour mid of the flight corridor. Dashed lines connect the sonde sectors. Background map made with Natural Earth.

its IVT ~~divergence for each sector respectively.~~ divergence, respectively (Fig. 5). ~~We~~ Inspecting the sonde positions in Fig. 5, we emphasise that our IVT-determined frontal AR sectors along the flight track tilt while the internal IVT ~~corridor~~ has a straight northward orientation~~in Fig 5. This putative inconsistency~~ . This arises from the north-eastward displacement of the AR filament over the course of the 2.5 h synthetic flight section (Sect. 2.1). Accordingly, Sect. 5 examines the extent to which sonde-based IVT divergence is affected by flight duration, as opposed to actually looking at the AR in an instantaneous snapshot.

3 Moisture transport in Arctic AR cross-sections and its variability

This section ~~investigates~~ examines the IVT variability ~~within~~ in our arctic ARs (Sect. 2.2) using the high-resolution CARRA (Sect. 2.1). First, we analyse the shape of IVT (and document the larger IVT variability compared to forcing ERA5). Next, we focus on the observability of prevailing AR moisture transport variability by discrete soundings, using the synthetic sondes (Sect. ~~??~~2.1.2). We determine the maximum distance between sondes needed to derive the total moisture transport in AR cross-sections accurately (Q1). Finally, we describe how coherence in moisture and wind speed contributes to moisture transport and its variability (Q2).

3.1 Shape of IVT across arctic ARs

~~As observed in mid-latitudes (Ralph et al., 2017), IVT through AR cross-sections is commonly bell-shaped. Here, we infer~~ We investigate whether arctic ARs feature the same ~~structure~~bell-shaped structure of IVT along their cross-sections as observed in mid-latitudes (Ralph et al., 2017), and to what extent sondes can reproduce the IVT cross-section. For AR1, Figure 6 illustrates the ~~cross-sectoral~~ cross-section IVT along the inflow flight leg. We recognise the bell-shaped IVT from both, CARRA and forcing ERA5. Within the cross-section centre which we declare as the AR core ~~(~~in Sect. 2.3~~)~~, CARRA, however, shows stronger moisture transport with a more pronounced IVT maximum $> 500\,\mathrm{kg\,m^{-1}s^{-1}}$. Moreover, CARRA resolves more

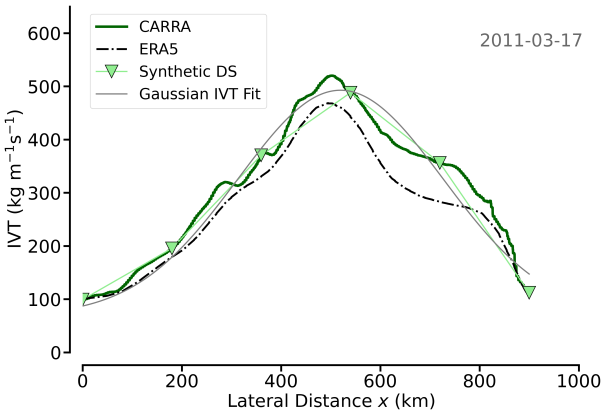

Figure 6. Inflow ~~AR-IVT~~ IVT cross-section from AR1 (2011-03-17) with six synthetic soundings placed along the track. A gaussian fit based on the sounding IVT representation is calculated (grey).

small-scale structures of the AR moisture transport. In particular, CARRA increases the cross-section variability for this case. ~~This increased lateral variability of IVT in CARRA arises the question, how sporadic soundings can reproduce such AR-IVT patterns. Using the synthetic soundings (Sect. 2.1.2) which consider CARRA as idealised reality, a set of six equidistant sondes would reveal a slightly different pattern of the AR cross-section in Fig. 6. A gaussian fit using the discrete soundings in a least-square sense can reproduce the bell-shaped distribution of AR-IVT. Yet, the fit is very sensitive to the actual positions of dropsonde releases. While the centred sonde in Fig. 6 is located close to the IVT maximum ($IVT_{\max}$), slight displacements of this release which easily occur in real observations, can rapidly cause an underestimation of the AR core moisture transport.~~Summarising all cross-sections of our ARs from Sect. 2.2, most arctic AR cross-sections ~~maintain the~~ show this typical bell-shaped IVT curve over widths of roughly 400–800 km and indicate pronounced IVT maxima in the core of 300–600 $\mathrm{kg\,m^{-1}s^{-1}}$ (not shown). Only for the weak AR8, this structure is less pronounced. We find that the arctic ARs are not substantially narrower than the AR widths of global climatology (Guan and Waliser, 2015) and observed mid-latitudes events (Cobb et al., 2021a). Flight planning should therefore consider cross-section distances of about 500-1000 km, similar to mid-latitude ARs. However, this only applies if the legs are not restricted to regions with $IVT > 250\,\mathrm{kg\,m^{-1}s^{-1}}$ which is a widely used threshold for mid-latitude ARs (e. g. Ralph et al., 2019). In contrast, the maximum IVT for the arctic events is roughly half as high as the majority of mid-latitude ARs from airborne studies in Cobb et al. (2021a). Moreover, the IVT magnitudes strongly differ between our cases and synoptic conditions. The strongest ARs, with $IVT_{\max}$ exceeding $500\,\mathrm{kg\,m^{-1}s^{-1}}$ are found for intense Greenland troughs, while the ARs are weaker along the Siberian pathway (see also Fig. 1). If we compare our ARs with those of other arctic case studies (e. g. Viceto et al., 2022), we are looking at rather strong ARs.

Viceto et al. (2022) documented the improved representation of arctic AR characteristics in ERA5 against coarser reanalysis data. In our comparison of CARRA with ERA5, the location and horizontal patterns of the ARs agree quite well (not shown). For all cross-sections, we ascertain plausible IVT values from CARRA with respect to ERA5. In particular, we highlight that

maximum (mean) values of IVT per cross-section increase by roughly 9 % (8 %) from ERA5 to CARRA on average. CARRA further increases the IVT variability by roughly 11 %. ~~This is an outcome of~~ We attribute this to the higher horizontal resolution than in ERA5. ~~While sonde~~

Using a set of six synthetic sondes, a gaussian fit of IVT can reproduce the bell-shaped AR-IVT cross-section (Fig. 6). This gaussian fit is very sensitive to the actual positions of dropsonde releases. While the centred sonde in Fig. 6 is positioned close to $IVT_{\max}$, a slight shift of this sounding, which easily occurs in real observations, can quickly lead to an underestimation of the moisture transport in the AR core. Flight planning should thus imply a sonde release in the vicinity of the predicted IVT maximum and place additional sondes symmetrically around the core. While sonde positions in Fig. 6 are suitable to represent the cross-section IVT, other ~~ARs signify~~ AR cross-sections evince more complexity in being accurately represented by this number of ~~placed~~ soundings. We need further inspections on how sounding intervals deteriorate the AR moisture transport observability.

3.2 Sonde-based total cross-section moisture transport

~~The most intuitive approximation of ∇IVT in AR corridors relies on deriving the $TIVT$ through the boundary legs. Following Ralph et al. (2017), $TIVT$ of a cross-section is defined as:~~

$$TIVT = \int IVT\, dx,$$

~~representing the lateral integral of~~ As stated in Sect. 2.3, the determination of $TIVT$ in two AR cross-sections can provide first estimates on the prevailing IVT ~~over the flight distance x in one boundary leg (in- or outflow). Assuming that no moisture flux exists apart from perpendicular to the flight track, we can approximate ∇IVT in an AR corridor by the difference of in- minus outgoing~~ divergence. However, the accuracy in sonde-based $TIVT$ ~~of the cross-sections. To assess the required sounding frequency, we vary the number of synthetic sondes .~~ of an AR cross-section depends on the number of sondes across the AR, i.e. their spacing (Ralph et al., 2017). For AR1, one of the stronger events with ~~$IVT_{\max} \approx 500\,\mathrm{kg m^{-1} s^{-1}}$~~ $IVT_{\max} \approx 500\,\mathrm{kg\,m^{-1}s^{-1}}$ (presented in Fig. 6), we find that from the release of six sondes ~~underestimates~~ we underestimate $TIVT$ by roughly 10 % against the continuous ~~AR-~~IVT representation in CARRA ~~.~~ (defined in Sect. 2.1.1). In contrast, $TIVT$ estimates based on ten sondes differ by less than 1 % (not shown). ~~When lowering the number of releases~~

For all of our AR events, we assess the required sounding spacing to gain adequate $TIVT$ estimates by varying the frequency between synthetic sondes and by comparing their values with $TIVT$ of the continuous representation in CARRA. When increasing the spacing between soundings, their location becomes more essential and strongly affects the derived moisture transport variability~~especially in the AR core with possible occurence of a low-level jet (LLJ). This sector accounts for $\approx 50\,\%$ of the entire moisture transport through the cross-section (Guan and Waliser, 2017). Too large sonde distances enhance the probability to miss this IVT dominating region. .~~ To account for this dependency, Figure 7 illustrates the outcome of a bootstrapping approach ~~wherein~~ in which we sample the cross-sections with varying release intervals and ~~positions. We apply this method to all arctic ARs (Sect. 2.2). The emerging boxplot (~~varying positions and derive $TIVT$ therefrom. The distributions of the relative error of $TIVT$ against the continuous AR representation (the grey box-whiskers in Fig. 7) ~~reveals how many sonde~~

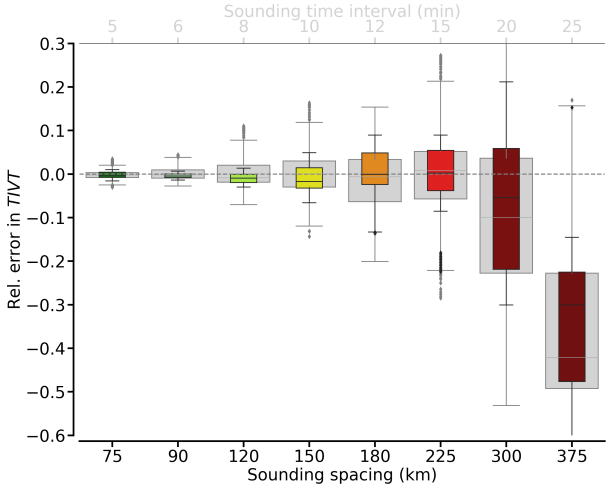

Figure 7. Relative error in $TIVT$ as a function of sounding ~~frequency~~ spacing in ~~seconds~~ km for all AR ~~cross-sections~~ cross-section representations (grey) and ~~colored,~~ those including highest ~~IVT maxima~~ (75th percentile) IVT maxima (coloured). Statistics rely on the boots-trapping approach containing of 100 cross-section sonde representations per AR. The boxes show the quartiles while whiskers show the rest of the distribution, except for outliers (markers). For an assumed aircraft speed of 250 m s^{-1}, ~~5 min (300 s) sounding spacing results in profile distances of 75 km (if sonde drifts~~ equivalent release intervals are ~~neglected)~~given on the top x-axis.

~~releases are needed to~~ reveal how dense sonde releases need to be performed in order to derive $TIVT$ in ~~our chosen ARs~~ the AR cross-sections ~~. Accordingly~~precisely. Correspondingly, the relative error of $TIVT$ against the continuous AR representation ~~starts to significantly increase for sounding intervals above 10 min (distances of~~ increases significantly for sounding spacing $\geq$ 150 km ~~at a cruise speed of 250 ms^{-1} and~~ (roughly five sondes for the given cross-section lengths~~). For intervals above 15~~, corresponding to release intervals above 10 min at a cruising speed of 250 m s^{-1}). For sonde spacing $\geq$ 200 km, sonde-based $TIVT$ can ~~strongly deviate. We find that~~ substantially deviate.

The $TIVT$ uncertainty in Fig. 7 increases less rapidly with larger sonde ~~intervals than in~~ spacing than derived for mid-latitude ~~case studies (~~AR cases (see Ralph et al., 2017 ~~;~~ and Guan et al., 2018)~~, but emphasise that our~~ . Total moisture transport in the arctic cases is, in turn, much smaller than in mid-latitude cases. The arctic $TIVT$ values ~~extend to roughly one third~~ are roughly half as high as the sonde-based mean $TIVT$ of ~~the~~ $5{\cdot}10^8$ kg s^{-1} ascertained by Ralph et al. (2017) from 21 mid-latitude ~~range of $8 - - 10 \cdot 10^8$ kg s^{-1}. We conclude that a minimum number of five releases must be targeted~~ARs. The ARs we consider have, in turn, roughly two third the width of the ARs in Ralph et al. (2017) and Guan et al. (2018). Here, we remind that our threshold to define the outer AR edges is much lower to encounter for arctic AR conditions. Applying the mid-latitude thresholds (given in Sect. 2.3), mean AR widths would be in range of a few hundred kilometer and $TIVT$ values much lower than in mid-latitude ARs.

~~The~~ With increasing spacing, the spread in $TIVT$ errors in Fig. 7 increases. One reason is the rising relevance of the sonde position. Too large sonde spacing enhances the probability to miss IVT ~~variability that causes such sonde errors in~~ dominating

regions. Especially with the occurrence of a LLJ, Guan and Waliser (2017) confirm that the AR core alone accounts for $\approx 50\,\%$ of the entire moisture transport through the cross-section. Yet, we also attribute the spread in relative $TIVT$ ~~is strongly correlated to~~ errors to the large AR case-to-case variability. In particular, the strong correlation of $IVT_{\max}$ to IVT variability (correlation coefficient $r = 0.91$) may cause sonde errors in derived $TIVT$. Hence, we expect ~~more sondes to be~~ that the smallest sonde spacing is required for the strongest AR events. However, the ~~coloured boxes in Fig. 7 indicate that the~~ distribution of the relative $TIVT$ error behaves similarly, when we ~~pick~~ refer to the cross-sections with $IVT_{\max}$ larger than the 75th percentile from the bootstrapping sample~~(mainly~~, mainly from AR1 and AR3 (coloured box-whiskers in Fig. 7) . The mean relative error increases more rapidly with larger ~~sounding intervals whereas the spread is lower than for~~ spacing whereas the inter-case spread is slightly lower than in the entire sample. ~~Highest~~ For sonde spacing ≥ 200 km, the mean error becomes slightly lower than in the entirety but more robust.

We conclude that highest $TIVT$ errors thus do not originate from the strong events when having very few sondes. ~~For larger sounding intervals (≤ 15 min), the mean error and its spread becomes lower than for the entirety.~~ Still, we emphasis that a minimum sounding spacing of 100-150 km has to be targeted for arctic ARs, which is less restrictive than for mid-latitude ARs in Ralph et al. (2017). In a larger set of arctic AR events than in this study, these recommendations for sonde spacing could be further specified in terms of arctic AR strength.

3.3 Variability of moisture and wind in arctic ARs

After investigating the overall moisture transport by its vertical integral IVT, ~~it is intuitive to~~ we take a deeper look at ~~vertical~~ moisture q and wind speed v (Eq. 1) individually ~~, and to compare arctic ARsto what we know from mid-latitude ARs. We examine~~ in order to address Q2 (Sect. 1). For all arctic ARs, Figure 8 examines the cross-section variability of v and q ~~in the vertical~~ over the vertical profile using the continuous ~~representation of our arctic ARs (Fig. 8). Moisture~~ AR representation (Sect. 2.1.1). Here, moisture transport in the lowest levels up to 850 hPa ~~contributes to IVT with~~ contains roughly 50 % of the IVT magnitude. Up to this height, both high moisture and wind speeds are predominant, with a local maximum of wind speeds around 900 hPa. Further upwards, wind speed ~~even~~ accelerates up to ~~15 – 30 m s^{-1} and~~ 20–30 m s^{-1} while the atmosphere dries with height. The height decreasing moisture leads to a decline of moisture transport. Through the entire troposphere, q ~~decreases with height, remaining~~ overall remains below 5 g kg^{-1} in our arctic ARs. ~~These characteristics~~

The vertical moisture characteristics in Fig. 8b) resemble soundings of ~~ARs over the North-East Pacific (Cobb et al., 2021b) . Still, we find some notable differences to~~ arctic early summer ARs at Ny-Alesund demonstrated in Viceto et al. (2022) who showed q values up to 5 g kg^{-1}. However, the winds in our AR cross-sections (Fig. 8a) are roughly twice as strong as given in the case study of Viceto et al. (2022). Note that the ground-based station from which Viceto et al. (2022) depicted soundings were basically located at the outflow edge of the AR (with $IVT \leq 250$ kgm^{-1}s^{-1}) on the Luv side. Winds from the east were orographically slowed down by the massif of Svalbard. In this sense, the marine arctic ARs we consider are undisturbed. This enables stronger winds whose magnitude is rather comparable to mid-latitude ~~ARs. Whilst low-level wind speed is comparable to that in the Pacific region (Ralph et al., 2004; Cobb et al., 2021a) , q is considerably lower. The wind profile behaves more homogeneous in the vertical than registered from sub-tropical/mid-latitude cases (Ralph et al., 2005;~~

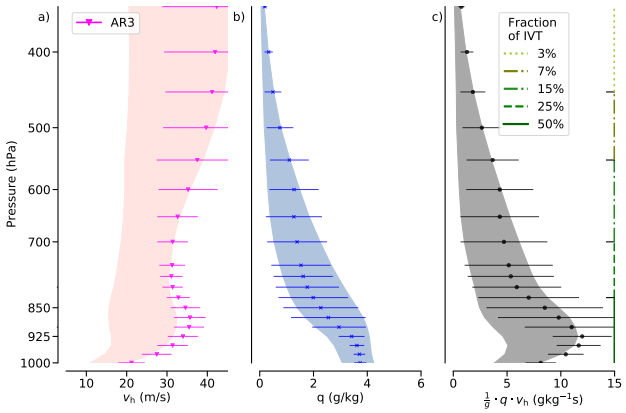

Figure 8. Vertical statistics of wind speed (a), specific humidity (b) and moisture transport (c) from the inflow cross-sections of the nine ARs analysed. Shaded areas represent the overall mean values ± the standard deviation. The error bars depict this distribution for the strongest AR (AR3). Vertical lines specify the cumulative contribution of moisture transport to IVT down to the given levels.

~~Cobb et al.,2021a). Above a slight bump~~ AR conditions. Ralph et al. (2004) and Cobb et al. (2021b) report on mean low-level wind speeds from 10–25 m s^{-1} for a large set of ARs over North-East Pacific. The slight local wind maximum at 900 hPa ~~, mostly designated as LLJ~~ (Fig. 8a) arises from the presence of strong wind corridors designated as LLJs that represent a common feature in mid-latitude ARs (Ralph et al., 2004; Demirdjian et al., 2020)~~, the wind speed slightly decreases before continues increasing. Since the atmosphere dries with height, the moisture transport declines~~. Their polar existence is verified in the case study of Terpstra et al. (2021). We find a very dominant LLJ inside our most intense AR (AR3 in Fig. 8). Above the local wind maximum, the vertical profile of wind speed remains more homogeneous than in sub-tropic/mid-latitude cases where Ralph et al. (2005) and Cobb et al. (2021a) registered a stronger intensification with height.

The ~~cross-sectoral~~ cross-section variability of both ~~quantities~~ moisture and winds strongly affects IVT variability. The shadings in Fig. 8 indicate that the standard deviation of moisture transport resembles the standard deviation of the winds for the lower levels up to 850 hPa, before moisture transport variability is apparently driven by the standard deviation of moisture in upper levels, although the wind standard deviation becomes highest above 500 hPa. ~~Figure 8 exemplarily depicts our most intense AR~~ For the most intense AR (AR3)~~. The LLJ in AR3 with~~ , the LLJ exhibits high wind speeds above 30 m s^{-1} ~~causes~~ that cause strong moisture transport whereas moisture is more or less average ~~.~~ (Fig. 8a). While strong moisture transport ~~originates from~~ in AR3 originates from overall strong winds, ~~its cross-sectoral variability is mostly affected by moisture variability. The strong AR3 suggests that moisture~~ moisture varies strongly and seemingly dominates the moisture transport variability ~~in arctic ARs, when windsare overall strong.~~ (Fig. 8b). Hence, we hypothesise that in strong arctic ARs with intense winds, moisture variability primarily steers IVT variability and leads to the bell-shaped IVT cross-section pattern depicted in Sect. 3.1.

~~Aiming at an~~ The identification of the more variable quantity ~~out of q and v~~ can improve measurement strategies. Specif-

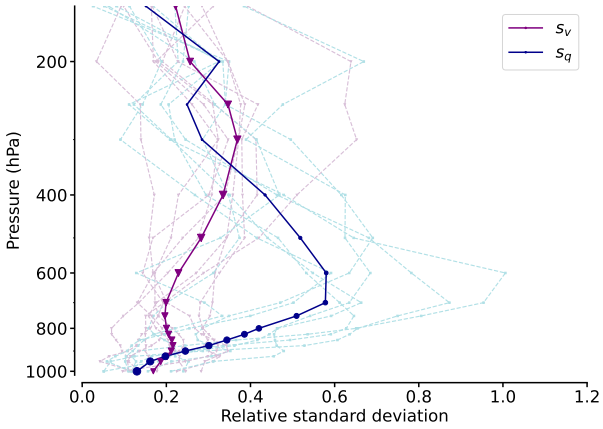

Figure 9. Vertical profile of relative standard deviation of wind (s_v) and moisture (s_q) for the AR cross-sections of each flight. The bold lines indicate the mean value over all ARs for both components. The sizes of the dots scale with the mean value at this height normed by the maximum mean value for the entire profile.

ically, moisture can be derived from supplementary remote sensing devices on ~~long-term research aircrafts. For wind and moisture~~long-range research aircraft. For this reason, we quantify the relative standard deviations of wind and moisture (s_q and s_v), ~~normed by the mean,~~ normalised by the horizontal mean. We investigate s_q and s_v as a function of height (Fig. 9). ~~In particular~~ Especially for the winds, the relative standard deviation in Fig. 9 remains rather consistent throughout the
545 ~~atmosphere and at~~ troposphere and has a small magnitude (mean relative variability around 20 to ~~30~~35 %)~~, which is in line~~. This is in accordance with the high but rather ~~homogenous winds in the strong~~ homogeneous wind speeds in AR3 (Fig. 8). Besides a weak local ~~maxima~~ maximum in the vicinity of the LLJ, the variability increases near the upper-level polar jet, ~~however,~~ but with minor impact on the moisture transport (variability) due to dry ~~airmasses~~air masses.

The variability of moisture behaves differently. In the boundary layer, moisture variability is negligible ~~,~~ similar to wind
550 ($s_q, s_v < 20\,\%$). Yet, the decline of mean moisture with height is opposed by ~~the~~ an increase of its relative variability. Between 600 and 850 hPa, high moisture variability~~basically contributes to mean moisture transport variability~~, increasing half as high as its mean~~. The cross-sectoral~~ , basically contributes to mean moisture transport variability. Based on our AR cross-sections, we conclude that moisture represents the more variable quantity in arctic ARs.

3.4 Coherence of moisture and wind

555 For the moisture transport, it is not only important whether moisture and wind anomalies are high separately (Sect. 3.3), but also how correlated they ~~are and whether coherent pattern~~ evolve along the AR cross-sections and whether connected patterns contribute significantly to AR-IVT (Q2). If ~~they~~ both patterns do, carefully collocated observations are essential to determine $TIVT$, otherwise independent estimates of mean moisture and wind are sufficient. The overall moisture transport $\overline{q \cdot v}$ ~~basically is~~ is basically a combination of transport by the mean quantities $\overline{q}$ and $\overline{v}$ and their ~~cross-sectoral variabilities~~correlated

cross-section variability, i.e spatial fluctuations q' and v', according to:

$$\overline{q \cdot v} = \overline{(\overline{q}+q')(\overline{v}+v')} = \overline{q} \cdot \overline{v} + \underbrace{\overline{q'\overline{v}}}_{=0} + \underbrace{\overline{\overline{q}v'}}_{=0} + \underbrace{\overline{q' \cdot v'}}_{\mathrm{cov}(q,v)} . \tag{6}$$

While the second and third summand equal zero, the last term represents the covariance cov() between q and v. ~~Vertical profile of relative standard deviation of wind (s_v) and moisture (s_q) for the AR cross-sections of each flight. The bold lines indicate the mean value over all ARs for both components. The sizes of the dots scale with the mean value at this height normed by the maximum mean value for the entire profile.~~ Using the relation between correlation coefficient r_{corr} and cov(), we obtain:

$$\mathrm{cov}(q,v) = r_{\mathrm{corr}}(q,v) \cdot \mathrm{std}(q) \cdot \mathrm{std(v)}, \tag{7}$$

and expanding by $\overline{q}$ and $\overline{v}$, we can reformulate Eq. 6 as:

$$\overline{q \cdot v} = \overline{q} \cdot \overline{v} \cdot \underbrace{(1 + r_{\mathrm{corr}}(q,v) \cdot \underbrace{\frac{\mathrm{std}(q)}{\overline{q}}}_{s_q} \cdot \underbrace{\frac{\mathrm{std}(v)}{\overline{v}}}_{s_v})}_{cov_{\mathrm{norm}}}. \tag{8}$$

The normalised covariance cov_{norm} (right summand in Eq. 8~~, the normalised covariance cov_{norm}, weights the~~) weighs the coherent transport relative to the non-coherent $\overline{q} \cdot \overline{v}$.

Using cov_{norm}, ~~we find~~ Figure 10 finds rather little coherence between moisture and wind in arctic AR cross-sections~~(Fig. 10).~~ . The magnitude of the contribution of moisture transport variability to the overall moisture transport is below $\pm 10\,\%$ for each height. Accordingly, the coherence is of minor influence for the entire IVT variability. Main reasons for the low contribution of coherent patterns are the relatively low standard deviations compared to their mean (see s_q and especially s_v). Even considerable correlation ($r_{\mathrm{corr}} \geq 0.5$, Fig. 10) cannot generate relevant moisture transport contributions. Over the vertical extension, cov_{norm} mostly remains below 5 %. Even in moisture transport dominated levels (below 700 hPa), the cross-sections reveal a contribution of moisture transport variability to Eq. 8 in the range of 5 to 10 %. Only for some ARs, the strongest variability ($> \pm 10\,\%$) primarily occurs in higher levels above 500 hPa, where, in turn, moisture transport is weak (Fig. 8 and Fig. 10). ~~As~~ The correlation between moisture and wind r_{corr} shows a large spread between the single ARs (grey lines in Fig. 10), ~~Figure 11 illustrate~~ so that we take a closer look into the spatial patterns of moisture and wind for our AR cross-sections ~~. As already shown for the mean r_{corr},~~ in Figure 11.

Inspecting the vertical AR curtains in Fig. 11, we recognise several features that we know from mid-latitude ARs. For instance, Ralph et al. (2004) and Cordeira et al. (2013) found the vertical slanted structure of moisture transport in AR cross-sections from dropsondes and reanalyses, where Ralph et al. (2017) verified the vertical interaction between the ~~correlation between moisture~~ upper-level jet and the LLJ that dominates the AR moisture transport. In Fig. 11, their conceptual depictions reflect mostly for AR5 and AR6 where moisture and wind are most coherent. Here, moist air masses residing in the warm conveyor belt are lifted over the cold-frontal sector. The downward intrusion of the upper-level jet on the eastern flank causes the slanted structure in the moisture transport. For the windy arctic AR events, e.g. AR3 and ~~wind peaks in the LLJ height ($r_{\mathrm{corr}} > 0.7$ for~~ AR5, we detect the presence of LLJs stronger than $25\,\mathrm{m\,s^{-1}}$. The LLJ is situated at a height of around 900 hPa, slightly

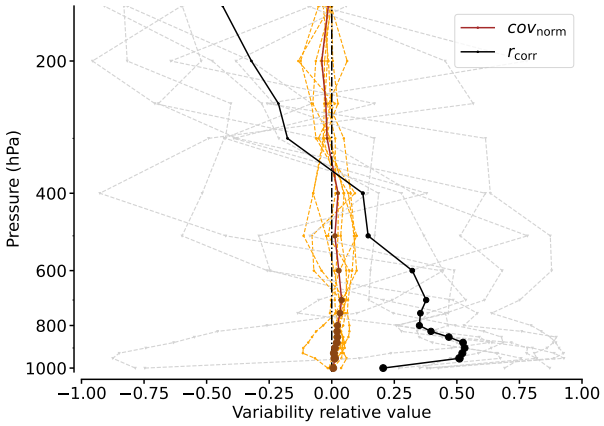

Figure 10. Vertical profile of AR moisture and wind normalised covariance (cov_{norm}) and their correlation r_{corr} along the cross-sections. The bold lines indicate the mean value over all AR for each of the components. The sizes of the dots scales with the mean moisture transport value at this height normed by the maximum mean value of the entire profile.

lower than Cobb et al. (2021a) summarised for mid-latitude ARs. In almost every cross-section (Fig. 11), the specific humidity exceeds $4\,\mathrm{g\,kg^{-1}}$ indicating that our events are rather moist for arctic AR conditions (e.g. Viceto et al., 2022), but much drier than mid-latitude ARs where q easily exceeds $8\,\mathrm{g\,kg^{-1}}$ (Cobb et al., 2021a).

Still, we notice a large case-to-case variability in Fig. 11 and partially less compliance to the conceptualised AR schematics illustrated in Ralph et al. (2017). This shows for the vertical structure of moisture, the presence and intensity of the LLJ (strongly distinctive in AR1, AR3, AR5, AR7, but missing in the other ARs) and how patterns of moisture and wind are correlated. Apart from AR5, other ARs exhibit less coherent patterns where wind and moisture do not necessarily align with each other. Especially AR9 indicates a clear horizontal displacement, causing a negative correlation along the cross-section. Here, subsiding dry air masses in the cold sector counteract the westward increase of wind speeds. For all ARs except for AR1, AR8 ~~, and AR9~~). ~~However, the variability of wind is small~~ , the correlation between moisture and wind peaks in the LLJ height ($r_{\mathrm{corr}} > 0.7$, Fig. 11). AR1 and AR3 exhibit small horizontal variability in the wind field, as winds are almost constant along the entire cross-section (~~$> 25\,\mathrm{ms^{-1}}$ especially in AR1 and AR3~~$> 25\,\mathrm{m\,s^{-1}}$). Here, it is the moisture variability steering the moisture transport variability. ~~Such moisture variable ARs~~The ARs, being variable in moisture, consist of an elevated moist ~~layer only persisting~~ plume only residing in the AR core ~~and~~ that is surrounded by dry air. The strength of dry air subsidence is primarily relevant for slanting the moisture transport along the cross-section. We find this most effective for ARs close to the dry air masses east of the Greenland coast (AR3) and when the backside of the embedded cyclone advects the dry Greenland air masses (AR9).

~~Cross-sections of AR inflow legs for moisture (color-coded contours), as well as wind contour lines for (pinkish) and moisture transport (both as contour lines). Shown moisture transport values have the unit $\mathrm{gkg^{-1}ms^{-1}}$. The black-white dashed vertical line represents the cross-sectoral mean of the correlation coefficient r_{corr} between moisture and wind for each pressure level.~~

~~The slanted structure of moisture transport in AR cross-sections (depicted in e.g. Ralph et al., 2004; Cordeira et al., 2013 Ralph et al., 2017) mostly reflects for~~ The variety of moisture transport characteristics comes with the very different synoptic patterns (troughs, ridges, smaller cyclones embedded in a meridional, but rather weak flow) causing the arctic ARs. In addition, we consider different corridors of the respective ARs. While AR5 ~~where moisture and wind are most coherent.Residing in~~ was mainly observed in the AR center, other ARs such as AR2-4 and AR7 are observed in the exit region of the AR (see Fig.1 and Fig. 2). Terpstra et al. (2021) detected that moisture and wind patterns and their coherence in polar ARs strongly change along the AR direction. In their case study, the ~~warm conveyor belt, moist air masses lift over the cold-frontal sector. The downward intrusion of the upper-level jet on the eastern flank causes the slanted structure in the moisture transport. Other ARs exhibit less coherent pattern and wind and moisture do not necessarily align with each other. For example, AR9 indicates a clear displacement causing a negative cross-sectoral correlation.~~ pronounced AR pattern, as depicted in Ralph et al. (2017), vanishes out more towards the Poles and the AR exit region. Similarly, the most textbook AR among our cases, AR5, is also the southernmost AR (Fig. 1). Moreover, Terpstra et al. (2021) identified decreasing coincidence between moisture and wind in the polar AR exit region. In their case, the LLJ resides in rather dry regimes below the local moisture maximum. While we detect this vertical separation of moisture and wind patterns mainly for AR4, but less uplifting of maximum moisture than in Terpstra et al. (2021), we emphasise the horizontal displacement of moisture and wind sectors in AR exit corridors (Fig. 11).

We conclude that ~~the~~ mean moisture and wind account for 95 % of overall moisture transport in arctic ARs. Moisture and wind patterns ~~are little coherent and~~ exhibit little coherence especially in arctic AR exit corridors, but show high inter-case variability. ~~Strong ARs ($IVT \geq 400\,\mathrm{kgm^{-1}s^{-1}}$~~Despite the variability, we postulate that strong ARs ($IVT \geq 400\,\mathrm{kg\,m^{-1}s^{-1}}$) tend to feature strong, but rather constant winds. ~~Narrowed moisture columns here form the~~ Instead, narrow and high-reaching moisture plumes in the core control moisture transport variability. ~~We recommend supplementary measurements of moisture to effectively increase the accuracy of AR moisture transport estimates.~~ The effectiveness of dry subsidence backwards the AR modulates the AR moisture transport pattern. An improvement for observing the moisture transport variability should thus be built upon supplementary moisture measurements rather than those of the winds. Incoherent cross-section patterns motivate investigating separate sectors along the AR front as they exhibit different processes (Cobb et al., 2021a). When moisture and wind ~~regimes are independent, we~~ patterns do not coincide, we can expect cross-frontal differences in the divergence components ~~of~~ (Eq. 5~~.~~).

4 Moisture transport divergence from sondes

~~After assessing how sondes reproduce moisture transport variability (Sect. 3), we focus on IVT divergence. This section examines~~ This section analyses how the divergence of moisture transport is characterised along cross-sections of arctic ARs (Q3). ~~We investigate whether high moisture advection~~ Resuming the decomposed terms (Eq. 5), we inspect whether high moisture advection occurs more frequently in strong moisture-dominated ~~ARs~~ AR sectors and whether mass convergence dominates in windy ~~AR corridors.~~ AR sectors. We categorise our results based on frontal sectors defined in Sect. 2.3. Synthetic

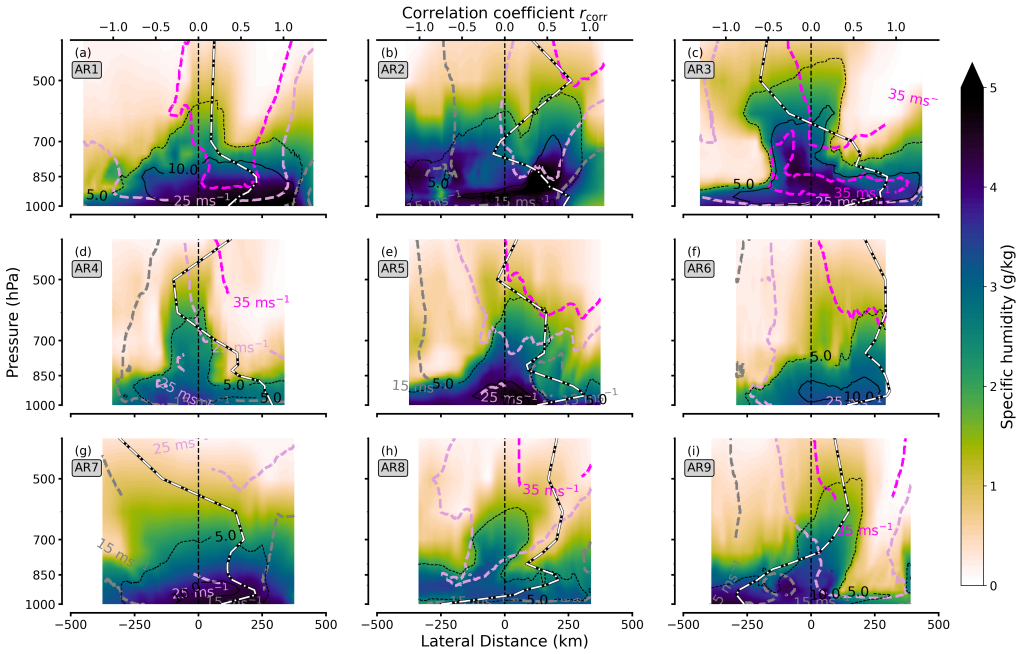

Figure 11. Cross-sections of AR inflow legs for moisture (color-coded contours), as well as wind contour lines for (pinkish) and moisture transport (both as contour lines). Shown moisture transport values have the unit $gkg^{-1}ms^{-1}$. The black-white dashed vertical line represents the cross-sectoral mean of the correlation coefficient r_{corr} between moisture and wind for each pressure level.

sondes illuminate how discrete soundings reflect such characteristics ~~.~~ against the continuous flight representation along the AR cross-sections (Sect. 2.1.1).

4.1 ~~Sectoral in-~~ In- and ~~outgoing moisture transport~~outflow *IVT*

In a first step, we depict the cross-sectoral Before coming to the moisture transport divergence at single levels, we compare the integrated quantities, namely cross-section IVT of the in- and outflow leg and their AR-$TIVT$ for all nine arctic ARs (Fig. 12). The leg comparison reveals a first simplified understanding of comparison of $TIVT$ in both legs reveals first simplified estimates of the prevailing divergence. Idealising that no entrainment into the AR corridor (Sect. 43) takes place, we can contrast Figure 12 contrasts $TIVT$ of the in- and outflow $TIVT$ in order to gain benchmarks cross-section to estimate whether convergence or divergence of internal moisture transport overall exists. Maximum moisture transport inside the AR corridor exists. Figure 12 indicates that maximum IVT values vary between 200–650 kg m^{-1}s^{-1}, whereby 200–650 kg m^{-1}s^{-1}, with the outflow IVT generally exhibits a similiar intensity as having a similar intensity to the inflow leg. The strongest AR in terms of maximum IVT also has the highest total transport throughout in both flight legs. Overall, $TIVT$ overall ranges from 100–300 $\cdot 10^6$ kg s^{-1}. Some arctic AR cross-sectoral 100–300 $\cdot 10^6$ kg s^{-1}. Recall that this is approximately one third to one half the $TIVT$ tends to decrease downstream. Higher IVT causing higher $TIVT$ in the inflow leg potentially suggests

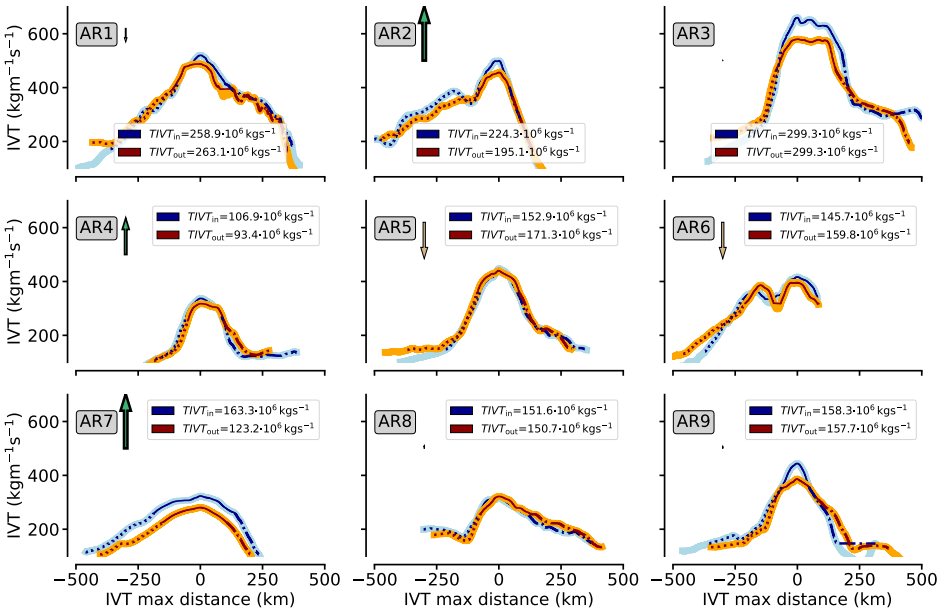

Figure 12. ~~AR-IVT of~~ IVT along inflow (outflow) ~~section~~ legs in blue (orange) for all nine ~~corridors~~ ARs (Fig. 1). Changes in line styles denote the ~~ARs. The domains of~~ frontal ~~specific AR sectors are denoted by the line pattern changing. Dotted~~ sector classifications (~~dashed~~Sect. 2.3): Dotted lines represent ~~the warm~~ cross-section periods attributed to pre-frontal ~~(cold~~ sectors, while dashed lines refer to post-frontal ~~)~~ sectors~~using the criteria mentioned in Sect~~. ~~2.2. Leg specific~~ The legend depicts $TIVT$ values for ~~AR-$TIVT$ are specified in~~ the ~~legend~~in- and outflow cross-section parts within the AR. They ~~purely~~ include IVT purely internal of ~~we declare as AR~~ determined AR borders ~~in~~ (Sect. 2.3~~(dotted lines~~). Arrows indicate the $TIVT$ difference between in- and outflow leg scaled in length and width. The differences can be viewed as simple estimates of IVT divergence in between both legs, according to Sect. 2.2. Upward (downward) ~~arrows roughly estimate corridor IVT~~ arrow scales represent estimated convergence (divergence) magnitudes. ~~Their length and width scales with~~ Note the ~~difference of $TIVT$ between both flight legs~~x-axis orientation is from east (left) to west (right).

~~total convergence in the AR corridor.Still, we identify cases with little streamward tendencies of total moisture transport and others that even show divergence. This downstream difference of $TIVT$ is distributed unevenly over the cross-sectoral IVT.~~ magnitude found in mid-latitude ARs (Ralph et al., 2017).

~~Figure 12~~ Figure 12 further separates the AR cross-sections in the three sectors (pre-frontal, core, post-frontal)~~as introduced in Sect. 2.3.~~. Although the AR cores are roughly 200–300 km narrow (slim lines in Fig. 12), they provide more than half of the entire AR-$TIVT$. This contribution of the AR core agrees with findings from Cobb et al. (2021a) in mid-latitude ARs. Except for AR2 and AR7, weaker slopes of IVT are generally in the cold sector as opposed to the warm sector. ~~The~~ In turn, the steep post-frontal IVT decline in AR2 and AR7 ~~suggests different evolution processes associated with a high pressure ridge, favoured by anticyclonic rossby wave breaking (Zavadoff and Kirtman, 2018). While we mainly find~~ results from calm air masses on the backside of the AR (see also Fig. 11).

Comparing both legs (Fig. 12), cross-section $TIVT$ tends to decrease downstream in some arctic ARs. Here, higher IVT

~~decreasing~~ and $TIVT$ in the inflow leg suggests potential convergence in the AR corridor. Yet, we likewise identify cases with weak stream-ward tendencies in total moisture transport or with slight increases. Moreover, the downstream difference of $TIVT$ is unevenly distributed over the cross-section IVT. It is mainly within the AR core where IVT decreases towards the outflow ~~core,~~ leg (e.g. AR3, AR9), thus suggesting internal convergence. However, counteracting behavior in the frontal sectors partially compensates the core and stream-ward decrease of IVT~~occasionally intensifies in the two frontal sectors . They partially overcompensate the core leading to downstream net $TIVT$ gain. Yet,~~ . Like in AR6, the increase of warm sector IVT towards the outflow conveys a seeming divergence. This is in contrast to the findings in Guan et al. (2020), where the pre-frontal sector is denoted as a region of moisture transport convergence. Nonetheless, although the IVT patterns of AR5 and AR6 (Fig. 1) allow slight divergence in the pre-frontal sector, we emphasize that a $TIVT$-based interpretation of predominant moisture transport divergence underlies strong idealisation~~; Neither it considers~~ . It considers neither moisture flow being ~~not flightperpendicular~~non-perpendicular to the flight, nor does it separate contributions of moisture advection and mass convergence. ~~The regression approach is required~~ Therefore, we insist on the regression approach from Sect. 2.2 to diagnose moisture transport divergence in each ~~sector of~~ frontal sector of the arctic ARs.

4.2 Sonde-based divergence and its representativeness

This section ~~specifies the regression-based (Sect. 2.2)~~ derives the IVT divergence (∇IVT) in arctic ARs, Using the regression-based approach (Sect. 2.2). The moisture transport divergence is specified for the frontal sectors (Sect. 2.3) ~~using~~ and for the decomposed terms, namely moisture advection ADV and mass convergence $CONV$ (Eq. 5). ~~We compare our ∇IVT with that based on the mid-latitude study of Guan et al. (2020). The results we obtain~~ Again, the results from the continuous ~~cross-sections interpolated from CARRA~~ cross-section flight legs (Sect. 2.1.1) represent our idealised reference. ~~For them and~~ We compare them to the results referring to seven synthetic sondes per cross-section (as in Fig. 5)~~, we apply the regression method to derive ADV and $CONV$. We build on the airborne study of Norris et al. (2020), investigating~~ . This comparison assesses uncertainties of sonde-based ∇IVT , representative for arctic AR conditions. In doing so, we build on Norris et al. (2020) who pioneered the airborne derivation of all AR moisture budget components, including moisture transport divergence, by sampling a mid-latitude AR event~~, and assess uncertainties of sonde-based determination of ∇IVT in arctic ARs~~.

~~For the intense AR3~~In a first step, Figure 13 delineates the divergence components ~~specified~~ for the frontal sectors within the intense AR3. In the continuous AR representation, ADV and $CONV$ ~~behave differently~~ exhibit different vertical profiles throughout the frontal cross-section ~~, as stated in Guan et al. (2020) and Norris et al. (2020). While $CONV$~~ (Fig. 13). Comparing moisture transport divergence in the sectors for the continuous representation, we see that values range from -3 to $+1 \cdot 10^{-4}\,\mathrm{g\,kg^{-1}s^{-1}}$. While moisture advection (ADV) does not rise above $\pm 1 \cdot 10^{-4}\,\mathrm{g\,kg^{-1}s^{-1}}$~~in the warm sector, ADV exceeds $\pm 2 \cdot 10^{-4}\,\mathrm{g\,kg^{-1}s^{-1}}$. The cold sector even shows dry advection ($ADV > 0$) in the lower atmosphere. The ADV dominance contradicts the case observed by Norris et al. (2020), where ADV was small compared to~~ , mass divergence ($CONV$~~. They, in turn, observed a more intense mid-latitude AR near its centre. Our corridors along the sea ice edge can be primarily attributed to the AR exit region as the centre is located southwards (see Fig. 2)~~) decreases below $-2 \cdot 10^{-4}\,\mathrm{g\,kg^{-1}s^{-1}}$. For AR3, the ~~moisture transport convergence (divergence) manifests in the warm (cold) sector when we integrate along the vertical axis (not shown). This is~~

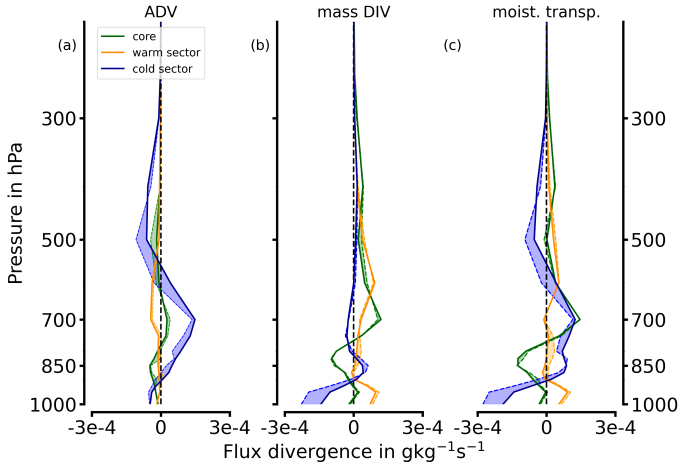

Figure 13. Vertical contributions from ADV (a) and $CONV$ (b) to ~~the~~ moisture transport divergence (c) for the frontal sectors in AR3. Bold lines represent ~~sonde-based values whereas~~ the ~~filled areas denote the deviation to values based on~~ continuous AR representation while dashed lines depict the sonde-based representation with the deviations as shadings.

~~similar to what is found in mid-latitudes (Guan et al., 2020). In AR3,~~ post-frontal sector is most crucial for moisture transport divergence. In detail, the warm pre-frontal sector and the core exhibit weak advection (Fig. 13a), whereas substantial advection occurs in the post-frontal cold sector. Similarly, the strongest mass convergence is found for the post-frontal sector (Fig. 13). Not only ADV and $CONV$ act ~~on~~ differently between the frontal sectors, they also dominate in different vertical levels. ~~Their maxima~~ The maxima of ADV and $CONV$ locate at the heights where also moisture and wind dominate ~~, respectively~~ (Fig. 11). ~~In the warm sector, moisture advection increases above 850~~While advection is predominant at mid-levels above 800 hPa ~~while mass converges closer to the surface and less intense. The core represents a transition zone with low-level moisture advection but significant drying in mid-levels (700~~up to 500 hPa, the mass divergence primarily acts below this level (Fig. 13 a and b). In the vicinity of the LLJ in the AR core at around 850 hPa~~)~~, predominant mass convergence (negative values) prevails, although the vertical column is slightly divergent in total. The advection of moisture in the prefrontal sector and core is too weak (Fig. 13a) to compensate the more prominent mass divergence (Fig. 13b). Overall, the moisture transport convergence (divergence) dominates in the cold post-frontal (warm pre-frontal) sector of AR3 (Fig. 13). We attribute the drying in mid-levels of the cold sector in AR3 to the dry cold air masses overrunning the AR behind the cold front (as also visible in Fig. 11c). The change in IVT direction behind the cold front (see Fig. 5) accounts for the low-level mass convergence in the post-frontal sector.~~The LLJ characterises a weak mass convergence maximum ($\approx -0.75 \cdot 10^{-4}$ g kg^{-1}s^{-1}) . The cold sector exhibits vertically consistent drying by advection (dominating) and mass divergence .~~

The fact that the moisture transport divergence components differ across the frontal axis is in line with mid-latitude AR based statistics of Guan et al. (2020). In detail, the characteristics in AR3 described above differ quietly to the AR case observed by Norris et al. (2020). In their airborne study of a mid-latitude AR, they found moisture transport convergence

to be strongest close the AR core and rather opposite signs for the pre- and post-frontal regions than us. Especially the lack of pre-frontal moisture advection in AR3, which Guan et al. (2020) actually robustly found in mid-latitude AR statistics, is worth-mentioning. In contrast to both Norris et al. (2020) and Guan et al. (2020), we do not identify a dominance of dynamical convergence over advection. The magnitudes of moisture transport divergence in AR3 are also much lower. Nonetheless, we remind that Norris et al. (2020) and Guan et al. (2020) consider even more intense mid-latitude AR near its centre. While AR3 is exceptionally strong for arctic conditions (Fig. 2), it is rather moderate for mid-latitude scales (Ralph et al., 2019).

Three synthetic sondes in each frontal sector leg (located as in Fig. 5) generally reproduce the divergence characteristics of the continuous reference within each ~~AR frontal sector .~~ frontal sector (Fig. 13). The highest deviations occur for the ~~warm~~ cold sector arising from ~~moisture advection misrepresentation. Slight~~ mid-level moisture advection and low-level mass convergence overestimation. We note that slight cross-sectoral displacements of the sonde positions ~~emerge in changing~~ deviate the divergence characteristics, but they ~~do~~ all maintain the principle vertical characteristics for each component and sector (Fig. 13). ~~Setting~~ When we contextualise our sonde results ~~in context to~~ with the airborne study ~~of Norris et al. (2020) , we identify~~ by Norris et al. (2020) using real dropsondes, we recognize the strength of real ~~dropsondes having~~ sondes with a high vertical resolution~~that provides much more~~ . They provide much greater vertical variability. Thus, ~~the lower divergence~~ it is likely that the quite low divergence displayed in Fig. 13 ~~presumably~~ does not only result from less ~~intense divergence in arctic ARs~~ divergence that prevails in arctic ARs compared to mid-latitude ~~ARs, but is also due to~~ ARs, but may also be a consequence of the coarser vertical ~~grid. To quantify the contribution of~~ resolution averaging out larger values. Nevertheless, given the before mentioned contrasts of AR3 to mid-latitude AR moisture transport divergence~~(such as in Fig. 13) to the moisture budget (Eq. 2), its~~ , we should involve our other AR events in order to pinpoint robust commonalities and differences to mid-latitude ARs, and to what extent the airborne sondes can reproduce them (Q3-Q4).

To compare moisture transport divergence for all our arctic cases with statistics of mid-latitude ARs, we derive the vertical integral ∇IVT ~~is required~~ (Eq. 5). This quantifies the contribution of moisture transport divergence to the moisture budget (Eq. 2). For our ARs, we summarise ~~their daily contribution to the moisture budget~~ the daily contribution of ∇IVT in mm d^{-1} (Fig. 14). ~~The~~ Accordingly, the warm pre-frontal sector overall supplies moisture ~~with advection being twice as dominant as convergence~~via advection that overcompensates weak mass divergence. In contrast, the core and post-frontal cold sector ~~clearly constitutes a moisture sink. The strongest drying is found here from mass divergence~~advection have a inter-case variability in the advection of either dry or moist airmasses. An overall large mass convergence in the post-frontal sector balances or even superimposes the advection. The post-frontal sector ~~exhibits~~ marks the highest inter-event variability. ~~The core marks the transition zone with positive and negative contributions prevailing for both components. Mass convergence shows a slightly stronger, more robust positive tendency. We note that the range of absolute values from -6~~Surprisingly, the mass divergence in the core shows a robust negative contribution for the moisture budget (Fig. 14).

For the arctic AR frontal sectors, the range of budget contributions from -3 mm d^{-1} to +43 mm d^{-1} ~~is pretty~~ in Fig. 14 is quite small compared to ~~Guan et al. (2020). In particular, the mass convergence is little compared to their~~ mid-latitude ~~cases (by a factor of 10). Hence, triggering of precipitation is presumably much less pronounced while moisture advection leads to an increase in~~ AR magnitudes. For statistics of mid-latitude ARs, Guan et al. (2020) summarises budget contributions in

the range -10 mm d^{-1} to +15 mm d^{-1}. The frontal characteristics of $CONV$ in arctic ARs contradict the understanding from Guan et al. (2020) who emphasized dominating mass convergence in and ahead of the AR front for mid-latitude AR. Unlike the mid-latitudes, the core of arctic ARs is characterised by the divergence of mass. This is surprising as our arctic ARs, like mid-latitude AR, contain LLJs, see again Fig. 11, which are associated with high mass convergence. This mass convergence is also found in many of our AR cases, but often superimposed by mid-level mass divergence above the LLJ. For the pre-frontal sector, moistening due to moisture advection is similarly identified for arctic (Fig. 14) and mid-latitude ARs (Guan et al., 2020) . In the post-frontal sector, both types of advection coexist, whereby the effectiveness of subsidence of dry air overrunning the AR in the ~~atmospheric moisture reservoir.~~ mid-levels becomes crucial (see also Fig. 11). High values in post-frontal mass convergence mainly arise from two AR cases (AR3, AR7), where low-level changes in wind direction induce the convergence of air masses (see also Fig. 1).

~~Box plot of moisture transport divergence contributions to daily moisture budget for all nine ARs. Values specify both components (ADV, $CONV$) for all frontal AR sectors. They compare the ideal AR representation (coloured box-whiskers) with the sonde-based values (grey box-whiskers). The boxes refer to the quartiles and horizontal lines inside specify the respective mean value. Applying three soundings per sector,~~ We emphasize that we cannot naively compare our frontal sector values with those of Guan et al. (2020). First, our arctic corridors along the ~~sondes replicate the cross-frontal divergence (grey whiskers in Fig. 14), i. e. the relatively weak mass convergence omnipresent for our arctic ARs. This contradicts Guan et al. (2020) who found dominating mass convergence in and ahead of the AR front. However, our values can not be intercompared naively. Besides our different AR regions (AR exit region at the~~ sea ice edge ~~that is more distant to the AR centre ,~~ are primarily attributed to the AR exit region as the centre is located more southwards (see Fig. 2)~~, our investigated~~ . For this exit region, we expect stronger divergence than convergence when the outflows of the ARs spread out. Guan et al. (2020) refer to the conditions across the AR centers. Second, our frontal sectors are larger than those classified by single reanalysis pixel-based values used in Guan et al. (2020). ~~In turn, our horizontal resolution includes subscale variability. Taking into account the observability~~ Our sectors are, however, more comparable among the AR events as they are AR relative and restrict to our defined AR edges. Note that the post-frontal sector in Guan et al. (2020) is also more distant and exclusive from the actual AR, where we would already consider dissimilar flow patterns, such as southerly flow backside of the cyclone in AR7. In their airborne case study, Norris et al. (2020) highlight that much higher values of moisture transport divergence occur at smaller scales than the reanalysis resolution used in Guan et al. (2020). Hence, we postulate that the sector-based values of moisture transport divergence ~~by discrete dropsondes, our~~ in Fig. 14 will also increase for smaller AR domains.

Applying three soundings per cross-section sector, the sondes replicate the cross-frontal divergence (grey box-whiskers in Fig. 14), i.e. the weak mass convergence being omnipresent for our arctic ARs. The sonde configurations derive similar median values as the continuous AR representation ~~. For our arctic AR composition, this confirms that three~~ and give evidence of the principle observability of moisture transport divergence by discrete dropsondes. Six sondes per sector are basically capable to reproduce the general frontal structure of moisture transport divergence and its vertically integrated contribution to the moisture budget. However, ~~as~~ the percentiles between sondes and the continuous representation deviate~~, the soundings~~ . For individual events, sondes can misinterpret the magnitude of ~~the~~ sector-specific divergence components considerably~~for~~

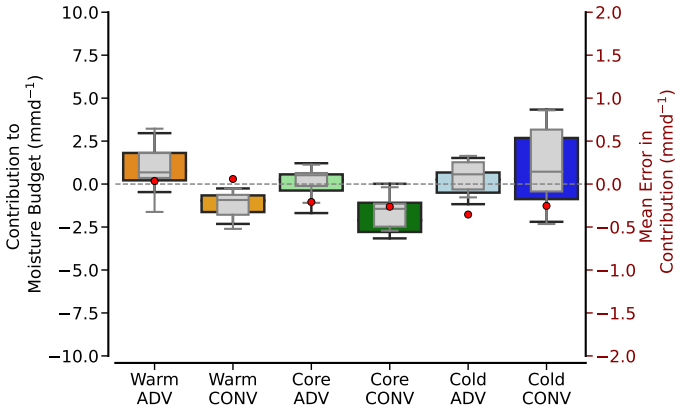

Figure 14. Box plot of moisture transport divergence contributions to daily moisture budget for all nine ARs. Values specify both components (ADV, $CONV$) for all frontal AR sectors (colour-coded). They compare the continuous AR representation (coloured box-whiskers) with the sonde-based values (grey). The boxes refer to the quartiles and horizontal lines inside specify the respective mean.

~~the individual events~~. Since this deviation is unbiased though, the sonde mean errors remain below 0.5 mm d^{-1} ~~. We remind that , while precedent moisture budget studies mostly refer to single time steps or at least conduct a time-to-space adjustment (Norris et al., 2020), we mimic the observations in the light of the~~ (Fig. 14).

Another aspect not touched on in our discussion so far is that we mimic all observations of moisture transport divergence in terms of flight duration. ~~The airborne~~ This is a major difference from Guan et al. (2020), who derived divergence components for individual reanalysis time steps. The airborne continuous realisation (Sect. 2.1.1) is non-instantaneous~~perspective can cause differences~~. This realisation can cause considerable deterioration in our understanding of the AR corridors ~~as the AR evolves meanwhile.~~

5 ~~Deterioration by non-instantaneous sounding~~

~~This section evaluates to~~ due to the temporal AR evolution meanwhile. This issue is also adressed in the airborne study of Norris et al. (2020), where they correct for the AR displacement over the flight duration by a time-to-space adjustment. However, they were not able to account for local temporal changes. Since our flight patterns cover larger AR corridors than in Norris et al. (2020), it is worth-investigating to what extent the ~~discrete synthetic sondes reproduce IVT divergence in the light of~~ temporal AR evolution during flight ~~(Q4). We quantify the error in observed moisture transport arising from the flight duration of up~~ may distort the airborne moisture transport divergence results.

5 Deterioration by non-instantaneous soundings

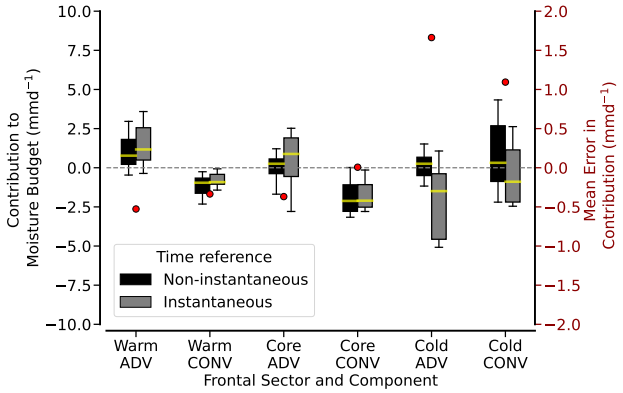

Figure 15. Comparison of divergence component contributions to daily moisture budget from spatially continuous AR representation referring to either evolving flight values (non-instantaneous) or to the values for the centered hour (instantaneous). Values are given for each frontal sector. Black error bars are identical to the coloured boxes in Fig. 14. Grey values represent centered hour-based values.

This section examines the extent to which the temporal AR evolution during flight affects the sonde-based representation of IVT divergence. Up to 3 ~~h to overpass AR corridors (Sect. 2.1.1), and to~~ hours are needed to fly over AR corridors and consecutively observe the in- and outflow ~~legs. Within the AR corridor, the~~ (Sect. 2.1.1). Meanwhile, temporal AR evolution ~~may deteriorate the airborne interpretation of Eulerian~~ can distort the airborne (non-instantaneous) representation of IVT divergence ~~. As instantaneous reference~~in the AR. Therefore, we establish ~~the~~ an instantaneous reference consisting of the spatially collocated AR representation ~~from CARRA~~ at the flight-centered hour ~~. Comparison of divergence component contributions to daily moisture budget from the continuous AR representation referring either on the time-propagating flight values or when using the values for the centered hour. Values are given for each frontal sector. Black error bars are identical to the coloured boxes in Fig. 14. Grey values represent the centered hour based values. In a first step~~and quantify the error in observed moisture transport that evolves over the flight duration. For the spatially continuous AR representation, we contrast the cross-frontal ∇IVT ~~for both continuous temporal representations~~ in both temporal perspectives (non-instantaneous and instantaneous). ~~On average for all cases, the frontal gradient~~

Summarising all ARs of Sect. 2.2, Figure 15 demonstrates that the frontal characteristics of ∇IVT ~~is well captured~~ are more or less reasonably reproduced by the non-instantaneous representation~~(Fig. 15).~~. However, we note that the mean non-instantaneous error in divergence ~~arising from~~ caused by the flight duration (red dots in Fig. 15) is ~~more pronounced~~ much greater than the error by ~~sonde-based undersampling~~ discrete sondes (compare to Fig. 14). In ~~some sectors, the~~ detail, the evolution of the ARs deviates the airborne estimates of moisture transport divergence by up to 25 % and even stronger on the backside of the AR. In the post-frontal sector, the mean error exceeds ~~more than 1 mm d^{-1}~~ 1.5 mm d^{-1}, whereas sonde undersampling (Fig. 14) only induces mean errors ~~below 0.5 mm d^{-1}~~ $\leq$ 0.5 mm d^{-1}. The temporal evolution of the AR throughout the flight can thus strongly deteriorate the divergence estimates for individual sectors. ~~Although both temporal representations identify moisture advection (ADV) as the dominating factor for moisture transport divergence, it~~ It is ADV in

the ~~core and~~ post-frontal sector where we find the highest deviations ~~($\geq \pm 1\,\mathrm{mm\,d^{-1}}$)~~ compared to the instantaneous snapshot (Fig. 15). The deviations show up in the mean, median and standard deviation. ~~In the cold~~ Not only does the instantaneous representation show more robust post-frontal ~~sector (core), the mean error and median of ADV consistently reveal more drying (moistening). Non-instantaneous sampling in instationary ARs changes the derived moisture budget contribution by more than 10~~dry advection than the airborne perspective, but there is also much greater case-to-case variability in its magnitude (-0.5 to -4 ~~%, especially for ADV in the cold-sector rising above 25 % (comparing mean errors on right axis to boxplot values in Fig. 15)~~ $\mathrm{mm\,d^{-1}}$) than seen from the aircraft. When we consider airborne (non-instantaneous~~deteriorations~~) deviations for individual ARs, we find cases with ~~ADV errors exceeding~~ errors in ADV that exceed more than $8\,\mathrm{mm\,d^{-1}}$ (not shown). ~~The~~ In the prefrontal sector and core, the median of $CONV$ is ~~much less affected. Relatively, however,~~ barely affected. Although $CONV$ ~~exhibits~~ has higher mean errors ~~but they have less impact~~ in relative terms, these have less influence on the absolute deviation of moisture transport divergence.

~~The before-mentioned error tendencies result from the slanted movement of the AR , not necessarily aligned with moisture transport direction. In fact, all our ARs evolve more or less northeastwards, while our flight pattern is more zonally orientated, aiming for transport-orthogonal~~ Referring to the ideal representation of ∇IVT in arctic AR cross-sections ~~. Since the winds exhibit less horizontal variability (Sect. 3.4), changes in mass convergence ($CONV$) which are lower than ADV remain less sensitive to non-instantaneous sampling and AR displacement. In-depth flight planning involving weather forecasts may help to adapt the flight pattern for AR evolution. Forecasts can estimate the mean propagation velocity and direction of the AR corridor center so that in- and outflow legs can be shifted.~~ that is instantaneous and spatially continuous, the divergence characteristics in the frontal sectors agree more with the mid-latitude statistics in Guan et al. (2020). In particular, we also identify a frontal gradient in the divergence components with overall moistening in the pre-frontal sector and drying in the post-frontal sector. In the arctic ARs, this is mainly driven by advection. Mass convergence being predominant in mid-latitude ARs is however missing or is at least superimposed by mid-level mass divergence.

Having ~~purely referred to the continuous sampling~~ just confined ourselves to the spatially continuous representations of moisture transport ~~before, we finally contrast the uncertainty arising from~~ divergence, we now contrast these with the sonde-based divergence resulting from the combination of non-instantaneous and discrete spatial sampling ~~by sondes and from non-instantaneous sampling in time.~~ (Sect. 4). Using the root-mean-square error (RMSE), ~~we compare the different~~ Figure 16 compares the different spatial samplings (continuous and discrete) in both time perspectives with our reference, the ~~continuous and~~ instantaneous representation. ~~The~~ Accordingly, the subsampling errors are minor ~~against the instationarity induced errors~~ compared to the errors induced by temporal evolution and cannot compensate the latter although they occasionally act in the opposite directions~~(Fig. 16). The~~ . The RMSEs for non-instantaneous ~~induced RMSEs~~ sampling are much higher ~~(up to more than $2\,\mathrm{mm\,d^{-1}}$) than the ones originating from spatial undersampling. While the~~ than the ones only induced by discrete sampling. Figure 16 underlines that the largest errors occur in the cold post-frontal sector. While the RMSE for the combination of non-instantaneous and discrete subsampling in the warm pre-frontal sector ~~shows the highest positive moisture budget contributions regardless of the error criteria (Fig. 15), this sector does not have the highest RMSE for both error sources (Fig. 16). The largest errors occur in the core and~~ and core is around or slightly below $1\,\mathrm{mm\,d^{-1}}$, the RMSE reaches up to $3\,\mathrm{mm\,d^{-1}}$

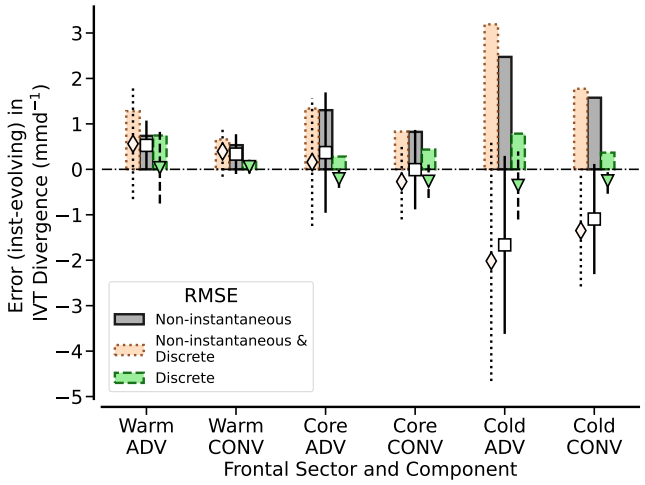

Figure 16. Total sonde error (orange) and individual errors ~~only~~ by only discrete sondes (green) and ~~only~~ by ~~instationarity~~ non-instantaneous sampling (grey) for daily IVT divergence in each frontal sector and divergence component (Eq. 5). For all AR cross-sections, positive bars indicate the root-mean-square error (RMSE) while error markers and lines depict mean errors in combination with their standard deviations for the ARs.

in the post-frontal sector. Non-instantaneous ~~sampling can misrepresent~~ discrete sampling by sondes misrepresents the divergence components by more than 50 % of the actual values (compare with Fig. **??**red

The values of moisture advection are more sensitive to airborne sampling than mass divergence values. In contrast to ~~sonde undersampling, instationarity-induced errors~~ discrete sampling, errors induced by instationarity in ADV act in a more consistent direction (error bars in Fig. 16). ~~Especially in~~ In the cold sector, AR instationarity mainly ~~causes an airborne underestimation in~~ leads to an underestimation of dry advection. ~~In the instantaneous reference, drier airmasses~~ These tendencies result from the oblique movement of the ARs which are not necessarily aligned with the moisture transport direction. In fact, our ARs move more or less to the northeast, while our flight pattern aims for cross-sections being orthogonal to the transport and are more zonally orientated. For the flight-centered hour (instantaneous reference), drier air masses are already more embedded in the post-frontal sector of the inflow cross-section ~~but differ~~ leg, but less in the outflow ~~transect. This gradient overall reinforces~~ leg. This changes the moisture gradient between both flight legs, increasing the overall dry advection. ~~Consequently, we generally expect~~ The winds exhibit less horizontal variability (Sect. 3.4). Temporal displacement thus varies $CONV$ less than ADV, so that $CONV$ remain less sensitive to non-instantaneous sampling.

We deduce that our flight pattern is subject to the strongest sonde-based misrepresentation in ∇IVT from advection in the cold post-frontal sector~~for such a zig-zag flight pattern.~~. Flight planning should involve weather forecasts to adapt the flight legs for AR evolution. Forecasts can estimate the mean propagation speed and direction of the AR corridor center so that in- and outflow legs can be shifted adequately. Similar to the error magnitudes, the inter-case variability in the divergence misrepresentation is much higher ~~in ADV.~~ for advection (Fig. 16). The large inter-AR variability ~~of the errors (Fig. 16)~~ in the results

highlights that more ~~cases~~ ARs should be considered in order to generalise the errors for arctic ARs. This includes differentiating ~~ARs~~ errors not only by ~~their~~ the AR strength, but by their AR corridor type (~~entrance~~entry, centre, exit). If ~~a zig-zag flight is more located in an intense AR centre~~flights are located in intense AR centres, we expect ~~the contribution of mass convergence and the~~ mass convergence to contribute more and errors due to ~~the sounding intervals to increaseso that $CONV$ becomes more comparable to Guan et al. (2020) and Norris et al. (2020)~~sounding spacing to increase. The mass convergence may be more similar to the mid-latitude values in Guan et al. (2020). However, ~~such AR conditions are rarely met close to~~ AR centers are rarely encountered near the sea ice in spring (Fig. 2). The ~~occurence of AR~~ occurrence of AR exit corridors over arctic sea ice is ~~considerably~~ significantly higher. This underpins the ~~usefullness of our benchmarks for dedicated arctic research flights~~ usefulness of our error estimates for research flights in arctic ARs. ~~This observability study investigates to what extent sporadic airborne dropsondes can represent the Integrated Water Vapour Transport (IVT) variability and its divergence inside~~

6 Conclusions and perspectives

This assessment study investigated the characteristics of the moisture transport divergence in arctic Atmospheric Rivers (ARs). We ~~elaborate on arctic AR conditions at the sea ice edge in Spring which have so far received less attention than mid-latitude ARs (e. g. Eiras-Barca et al., 2018; Ralph et al., 2019; Cobb et al., 2021a; Eiras-Barca et al., 2021). Since sophisticated airborne observations for arctic ARsdo not yet exist, we make use of the high-resolution CARRA reanalysis. The AR representation in CARRA forms our idealisation of the reality (that outperforms the AR-IVT ERA5 variability) to estimate the background IVT variability in arctic ARs. In CARRA, we locate zig-zag flight patterns to cover the~~ analysed the ARs from an airborne perspective to assess the dropsonde-based observability of moisture transport divergence of arctic AR. We characterised airborne uncertainties in sonde-based representation of the AR moisture transport divergence inside arctic ARs, focusing on two sonde-based limitations: subsampling by too large sounding spacing and the instationarity of the AR over the flight duration. For this, we followed a synthetic approach using reanalysis data as virtual truth. CARRA reanalysis data were interpolated on synthetic flight patterns that consist of two cross-sections covering frontal sectors over the entire AR transect. ~~The CARRA values are spatiotemporally interpolated onto the flight track.~~ Single vertical profiles ~~represent our synthetic dropsondes. The divergence is derived by regression methods (Stevens et al., 2019). We characterise uncertainties using dropsondes to monitor the AR moisture transport divergence. The synthetic sondes quantify the impacts resulting from discrete subsampling for IVT variability and their divergence representation. Second, sonde profiles along flight patterns are non-instantaneous~~emulate dropsondes.

We considered nine arctic AR events over the Atlantic pathway to the Arctic ocean in the vicinity of the sea-ice edge from last decade. The values of Integrated Water Vapour Transport (IVT) in the AR cores range from 300–600 $\mathrm{kg\,m^{-1}\,s^{-1}}$, although the ARs are primarily examined north of their center. We thus ~~elucidate how sonde-based~~ classify these ARs as overall strong for arctic conditions. Still, the bell shape of IVT ~~accuracy can be deteriorated by displacement and evolution of the AR over the flight duration. Our investigation of AR moisture transport in CARRA marks a detailed analysis of arctic AR-IVT expanding on mid-latitude studies of AR moisture budget (Guan et al., 2020). Using finer reanalyses manifolds our understanding of arctic~~

~~moisture transformation and will facilitate disentangling key processes of AR precipitation efficiency. Still, we are aware that our airborne emulation does not maintain all physical equilibria within the reanalysis. Considering corridors in nine arctic ARs in the vicinity of the sea ice edge, we rather intend to determine~~ across the AR varies strongly in between the AR cases. The considered cases cover a large variability and consist of various synoptic patterns (extended troughs, blocking situations, single cyclones) in which the AR are embedded. This study delivers benchmarks of uncertainties in the airborne representation of sonde-based AR moisture transport divergence~~, steming from sonde undersampling and the flight duration. This synthetic assessment concludes~~ . We conclude the four pursued questions (Q1-Q4) as:

What is the maximum distance between sondes to determine the total moisture transport through AR corridors? (Q1)

- For the ~~Total Integrated Water Vapour Transport ($TIVT$) of~~ sonde-based determination of Total Integrated Water Vapour Transport (in arctic AR cross-sections, sonde ~~distances~~ spacing below 100 km ~~have to be envisioned to certainly keep~~ robustly keeps $TIVT$ errors below 10 % ~~.~~ (Fig. 7). In strong ARs with IVT exceeding 500 kg m^{-1}s^{-1}, too coarse IVT representation at the AR core leads to $TIVT$ underestimation. Gaussian fits help ~~reproduce the cross-sectoral~~ to reproduce the cross-section IVT shape but are sensitive to how sondes estimate maximum IVT and its location. ~~We~~ Thus, precedent flight planning should aim for a sonde release at the forecasted IVT maximum and place additional sondes symmetrically around. For arctic AR widths of 400–800 km, we suggest a minimum of ~~five~~ seven soundings per cross-section ~~to~~ (roughly 60 to 120 km spacing) to derive $TIVT$ in both ~~boundary legsas first estimate of~~ cross-section legs. The maximum IVT ~~divergence appropriately~~is more correlated to IVT variability than the AR width is. The planning of sonde releases should thus rely on the steepness of IVT along the cross-section. We highlight that the differences of $TIVT$ between the in- and outflow cross-sections are in a range of 2–15 % (Fig. 12). If we want to reliably estimate moisture transport divergence based on $TIVT$ from both cross-sections, the sonde-based uncertainty of $TIVT$ for a single flight leg must be considerably lower.

How correlated are moisture and winds in arctic ARs and do coherent patterns contribute significantly to IVT? (Q2)

- ~~The cross-sections do not universally indicate coherent moisture and wind patterns. Both variables can be poorly correlated due to spatial separation. Maximum contributions of moisture and wind to IVT and its lateral variability act on different vertical levels. Moisture variability remains relevant up to about 700 hPa, when the AR core implies elevated moist layers. Wind variability is more crucial below~~ Moisture and wind in arctic ARs along the flight transects are only moderately correlated with mean correlation coefficient of 0.5 at about 850 ~~hPa. While lateral moisture transport variability contributes less~~ hPa height and less below and above. At the same time, the standard deviation of both quantities is smaller than its mean respectively. Moderate correlation and limited variability result in a small contribution of coherent patterns to IVT, which is smaller than 10 % ~~to its mean, the relative variability of both quantitiesrespectively is higher. In a relative sense, the variability of moisture dominates. For instance, our strongest AR characterises high moisture variability , whereas strong winds with little variability causes the transport of an overall rather small amount of moisture. We~~ of the moisture transport by the mean quantities. We draw the conclusion that collocated sampling of wind and moisture to assess the coherent transport is not of first priority. It is worth noting that the moisture variability

dominates the wind variability over most of the profile between 850 and 500 hPa. Only close to the surface, the wind variability peaks at about 850 hPa and plays an essential role. Thus, we prioritise supplementary airborne measurements of moisture to better represent arctic AR-IVT variability. ~~Unlike our northern cases, which are located more in the AR exit region, we expect wind variability to increase in corridors closer to the AR centre.~~

How ~~does~~ can the divergence of moisture transport ~~characterise~~ be characterised along ~~the cross-section~~ cross-sections of arctic ARs? (Q3)

– By ~~comparing~~ contrasting the in- and outflow ~~IVT through the AR transects, we overall expect~~ $TIVT$ through both cross-sections of all ARs, we expect an overall divergence in moisture transport. ~~However, ARs exhibit frontal-specific~~ Yet, the ARs show frontal specific characteristics in IVT divergence~~that~~, which have to be ~~decomposed to~~ separated into moisture advection (ADV) and mass convergence ($CONV$), see Sect. 4. The pre-frontal AR sectors contribute to the moisture budget via ~~both decomposits, whereas~~ moisture advection, while the post-frontal sectors ~~overall indicate divergence. The core represents the zone of transition.~~ generally show dry advection, but also occasional mass convergence. However, in contrast to mid-latitude ARs, mass convergence is much less dominant in the Arctic ARs. Although the mass convergence is generally dominant, especially below 850 hPa, it is often superimposed by upper-level divergence. In turn, moisture advection is much more relevant and dominates at levels higher than 850 hPa. Across the front, the total contribution of IVT divergence ~~overall contributes~~ to the moisture budget ~~by~~ is up to +~~4~~ 3 (pre-frontal ~~convergence) to −8 mm d^{-1}~~ moisture advection) to -3 mm d^{-1} (post-frontal ~~divergence~~dry advection). This is ~~of half~~ less than half the magnitude compared to the ~~mid latitudes, but of high intensity for the Arctic. We generally find mass convergence dominating mainly below 850 hPa, while moisture advection governs above. Mass convergence is much less relevant than moisture advection.~~ mid-latitudes.

To what extent can ~~discrete~~ non-instantaneous sondes reproduce IVT divergence in the light of AR evolution during flight? (Q4)

– Three sondes per frontal sector leg ~~can~~ are capable to reproduce the frontal ~~gradient of~~ characteristics of moisture transport divergence components with similar magnitudes~~of budget contribution (decline) in the pre-frontal (post-frontal) sector~~. The mean absolute error to the ~~idealised AR representation~~ continuous AR representation along the flight extends to around 0.5 mm d^{-1} ~~.~~ (Fig. 14). Sonde-based estimates are most sensitive in the post-frontal sector, where we also detect steeper gradients in moisture and winds than in the pre-frontal sectors. There is, in turn, high inter-case spread with positive and negative deviations. ~~Sonde-based moisture advection turns out to be more sensitive. Nonetheless, the undersampling error~~ Noteworthy is that the error for moisture transport divergence by undersampling becomes minor compared to the ~~flight duration induced error~~error induced by the flight duration. For the ~~AR core and~~ post-frontal cold sector, the temporal ~~AR~~ AR evolution during the flight ~~accounts~~ is responsible for more than twice ~~as high errors~~ the deviations in ADV ~~. Arising~~ and $CONV$. The divergence errors can exceed 50 % of the actual values. ~~In contrast to undersampling , errorsinduced by~~ Unlike the undersampling errors, non-instantaneous sampling ~~have~~ induces errors in a more consistent direction. ~~For determined mass-convergence, errors remain small with the lowest differences occuring~~

~~in the pre-frontal (warm) sector.~~ Especially in the post-frontal sector, the divergence is stronger for both, ADV and $CONV$ than assumed by the sondes. Here the intensity and pace of dry intrusions on the backside of the AR front plays a fundamental rule in the distortion of airborne sonde-based moisture transport divergence estimates. We conclude that moisture advection on the arctic AR ~~boundaries is both~~ edges is most contributing to the moisture transport divergence and in the post-frontal most sensitive to the airborne strategy as the ARs do not necessarily displace along the moisture transport direction. Although mass convergence is much less predominant than in mid-latitude ARs, directional convergence becomes relevant in the post-frontal sector, but is overestimated by sondes during flight.

~~Overall, we~~ We confirm the observability of moisture transport divergence in arctic AR corridors by releasing sondes in such dedicated flight patterns. A ~~minimum of seven sondes per~~ maximum sonde spacing of 100 km within the AR cross-section can ~~prinicpally~~ in principle characterise the divergence ~~under~~ between both cross-sections with the given uncertainties of ~~$\approx 10\,\%$. They determine divergence in a way that they cover cross-frontal gradients. The entire~~ $< 10\,\%$. For the flight duration, we obtain the moisture transport divergence ~~can be obtained~~ specified for frontal sectors with an uncertainty ~~lower than 25~~in the range of 25–50 %. We ~~emphasise the higher importance of supplementary measurements for moisture when~~ deduce that sonde undersampling matters and recommend a sequence of at least seven sondes per section given the widths of arctic ARs . However, notwithstanding that we could release a higher number of sondes, it is the temporal evolution of the AR over the flight duration that leads to higher deviations in the divergence components rather than sonde undersampling. The dedicated planning of such sonde-based purposes should not only include the positioning of the sondes, but also the minimisation of the flight duration. The placement of cross-section legs and their spacing should carefully consider the AR displacement during flight. Shorter distances between the cross-sections not only reduce the flight duration, but also the area enclosed by sondes. Given the frontal-sector widths of the arctic ARs, both cross-sections should be no more than 200 km apart. For several of our cases, the meridional separation is higher and we have to expect considerable subgrid scale variability. Collocated flights by two aircraft, with both cross-sections being not far apart and sampled simultaneously, is the optimal and still feasible strategy. When faced with a limited ~~amount~~ number of dropsondes, ~~as moisture represents the more varying quantity in our~~ supplementary measurements of moisture should be prioritised, as moisture is the more variable quantity and moisture advection mostly dominates the moisture transport divergence in the arctic AR corridors.~~Since our results mainly rely~~

Additional limitations of our study need to be discussed. As our results are mainly based on corridors in the AR exit region, we strongly recommend ~~an extension of~~ extending our uncertainty assessment to other AR regions ~~, and postulate~~ and expect the role of winds and mass convergence to increase in strong ~~ARs moving more poleward. This emerges as~~ AR centers. This becomes an even more ~~hot topic~~ important issue with respect to ~~polar ARs tending~~ the tendency of arctic ARs to shift more northward and ~~intensifying~~ intensify under climate change (O'Brien et al., 2022). ~~Our provided orders of magnitudes for IVT variability and divergence are representative for~~ Furthermore, as we include a large variability of synoptic AR patterns but a small sample, we propose statistics with a larger number of AR events. The statistics can improve our understanding of the moisture transport divergence patterns in arctic ARs and ~~quantify benchmarks in dropsonde-based derivation. Consistently mimicking the soundings is a fundamental stepstone to achieve an understanding of the uncertainties when such airborne tactics will actually be performed~~attribute it to the dynamic and thermodynamic atmospheric conditions. Here, CARRA represents a

very suitable reanalysis framework for this purpose in follow-up studies. Again, we encourage the use of the higher vertical resolution of the model levels rather than our chosen pressure levels, although sufficient for initial estimates. For real sondes, we ~~highlight~~ emphasise the added value of ~~the~~ their high vertical resolution. Sondes ~~reveal more precise information of~~ provide more accurate information on the vertical composition of ADV and $CONV$. ~~We deduce that sonde undersampling matters and recommend a sequence of at least seven sondes per cross-section. Yet, notwithstanding that we could release a much higher number of sondes, it is the temporal AR evolution over flight duration that leads to higher deviations in divergence components rather than sonde undersampling.Thus, dedicated planning of such~~ The sonde-based ~~observation purposes should not only involve dropsonde positioning but rather pursue minimising the flight duration. We postulate collocated flights where both~~ approach is limited to regression-based divergence where we consider only rather large areas and open meridional boundaries. Even with continuous lateral sampling, the meridional gradients are only coarsely sampled.

Therefore, a follow-up study should investigate how the arctic AR moisture transport divergence acts inside the flight corridor at grid-cell scales. This will allow two additional research topics to be addressed: First, the internal variability between both cross-sections ~~are sampled simultaneously by two aircraft as the optimum and still feasible strategy~~can be derived more precisely to improve the flight pattern, second the actual scales at which the moisture transport divergence varies significantly can be evaluated. This may also increase the divergence magnitudes, similarly to Norris et al. (2020) who found larger values of the divergence components. They considered smaller airborne AR corridors than the ERA-Interim pixels referred to in Guan et al. (2020).

Despite the aforementioned limitations, the orders of magnitudes for IVT variability and divergence that we provide are representative for arctic ARs and quantify benchmarks in the sonde-based derivation. Consistently mimicking the soundings is a fundamental step towards the understanding of the uncertainties when such airborne tactics are actually carried out. The benchmarks are not only useful ~~to improve~~ for improving flight strategies, but also indicate deviations in corresponding model-observation comparisons. Only ~~when we illuminate the constraints of~~ by illuminating the constraints on the AR representation from both models and observations, we establish a framework from which airborne observations can support modellers in terms of the resolution and complexity required for ~~parametrizations~~ parameterisation of moisture transformation processes caused by IVT divergence in arctic ARs.

Code and data availability. The code created by HD analysing the downloaded reanalyses and creates the figures can be accessed via github and is made available under: https://github.com/hdorff94/Synthetic_Airborne_Arctic_ARs. The reanalysis data from CARRA (Schyberg et al., 2021) and ERA5 (Hersbach et al., 2018) were accessed from the Copernicus Climate Change Service(C3S) Climate Data Store (CDS). The AR catalogue (Guan, 2022) used to pre-identify AR events of interest is provided by Bin Guan via https://ucla.box.com/ARcatalog.

Author contributions. HD, FA and HK were main initiators for the work in the scope of this manuscript. FA, HK and VS helped to conceptualise the manuscript. HD conducted the analysis presented and drafted the manuscript under scientific supervision of FA, HK and VS. All authors contributed to revising the manuscript.

Competing interests. The authors declare that they have no conflict of interest.

Acknowledgements. This study was supported by the Deutsche Forschungsgemeinschaft (DFG; German Research Foundation) under the HALO SPP 1294. We thank the two anonymous reviewers, for providing us with helpful comments that improved the quality of the paper, and the associate editor Geraint Vaughan. We explicitly acknowledge the Copernicus Climate Change Service (C3S) Climate Data Store (CDS) for providing access to CARRA and ERA5 data. We thank Bin Guan for making the AR catalogue publically available via https://ucla.box.com/ARcatalog. Furthermore, we want to thank Melanie Lauer and Geet George for various helpful discussions. Henning Dorff is thankful to Jochem Marotzke and Dallas Murphy for providing fruitful comments on the writing style and structure of the manuscript. Thanks also go towards Norbert Noreiks for delivering sketches of the research aircraft.

References

Bengtsson, L., Andrae, U., Aspelien, T., Batrak, Y., Calvo, J., de Rooy, W., Gleeson, E., Hansen-Sass, B., Homleid, M., Hortal, M., Ivarsson, K.-I., Lenderink, G., Niemelä, S., Nielsen, K. P., Onvlee, J., Rontu, L., Samuelsson, P., Muñoz, D. S., Subias, A., Tijm, S., Toll, V., Yang, X., and Køltzow, M. Ø.: The HARMONIE–AROME Model Configuration in the ALADIN–HIRLAM NWP System, Monthly Weather Review, 145, 1919–1935, https://doi.org/10.1175/mwr-d-16-0417.1, 2017.

Bony, S. and Stevens, B.: Measuring Area-Averaged Vertical Motions with Dropsondes, Journal of the Atmospheric Sciences, 76, 767–783, https://doi.org/10.1175/jas-d-18-0141.1, 2019.

Cobb, A., Michaelis, A., Iacobellis, S., Ralph, F. M., and Monache, L. D.: Atmospheric River Sectors: Definition and Characteristics Observed Using Dropsondes from 2014–20 CalWater and AR Recon, Monthly Weather Review, 149, 623–644, https://doi.org/10.1175/mwr-d-20-0177.1, 2021a.

Cobb, A., Monache, L. D., Cannon, F., and Ralph, F. M.: Representation of Dropsonde-Observed Atmospheric River Conditions in Reanalyses, Geophysical Research Letters, 48, https://doi.org/10.1029/2021gl093357, 2021b.

Cobb, A., Ralph, F. M., Tallapragada, V., Wilson, A. M., Davis, C. A., Monache, L. D., Doyle, J. D., Pappenberger, F., Reynolds, C. A., Subramanian, A., Black, P. G., Cannon, F., Castellano, C., Cordeira, J. M., Haase, J. S., Hecht, C., Kawzenuk, B., Lavers, D. A., Murphy, M. J., Parrish, J., Rickert, R., Rutz, J. J., Torn, R., Wu, X., and Zheng, M.: Atmospheric River Reconnaissance 2021: A Review, Weather and Forecasting, https://doi.org/10.1175/waf-d-21-0164.1, 2022.

Cordeira, J. M., Ralph, F. M., and Moore, B. J.: The Development and Evolution of Two Atmospheric Rivers in Proximity to Western North Pacific Tropical Cyclones in October 2010, Monthly Weather Review, 141, 4234–4255, https://doi.org/10.1175/mwr-d-13-00019.1, 2013.

Dacre, H. F., Martínez-Alvarado, O., and Mbengue, C. O.: Linking Atmospheric Rivers and Warm Conveyor Belt Airflows, Journal of Hydrometeorology, 20, 1183–1196, https://doi.org/10.1175/jhm-d-18-0175.1, 2019.

Dee, D. P., Uppala, S. M., Simmons, A. J., Berrisford, P., Poli, P., Kobayashi, S., Andrae, U., Balmaseda, M. A., Balsamo, G., Bauer, P., Bechtold, P., Beljaars, A. C. M., van de Berg, L., Bidlot, J., Bormann, N., Delsol, C., Dragani, R., Fuentes, M., Geer, A. J., Haimberger, L., Healy, S. B., Hersbach, H., Hólm, E. V., Isaksen, L., Kållberg, P., Köhler, M., Matricardi, M., McNally, A. P., Monge-Sanz, B. M., Morcrette, J., Park, B., Peubey, C., de Rosnay, P., Tavolato, C., Thépaut, J., and Vitart, F.: The ERA-Interim reanalysis: configuration and performance of the data assimilation system, Quarterly Journal of the Royal Meteorological Society, 137, 553–597, https://doi.org/10.1002/qj.828, 2011.

Demirdjian, R., Norris, J. R., Martin, A., and Ralph, F. M.: Dropsonde Observations of the Ageostrophy within the Pre-Cold-Frontal Low-Level Jet Associated with Atmospheric Rivers, Monthly Weather Review, 148, 1389–1406, https://doi.org/10.1175/mwr-d-19-0248.1, 2020.

Dufour, A., Zolina, O., and Gulev, S. K.: Atmospheric Moisture Transport to the Arctic: Assessment of Reanalyses and Analysis of Transport Components, Journal of Climate, 29, 5061–5081, https://doi.org/10.1175/jcli-d-15-0559.1, 2016.

Eiras-Barca, J., Ramos, A. M., Pinto, J. G., Trigo, R. M., Liberato, M. L. R., and Miguez-Macho, G.: The concurrence of atmospheric rivers and explosive cyclogenesis in the North Atlantic and North Pacific basins, Earth System Dynamics, 9, 91–102, https://doi.org/10.5194/esd-9-91-2018, 2018.

Eiras-Barca, J., Ramos, A. M., Algarra, I., Vázquez, M., Dominguez, F., Miguez-Macho, G., Nieto, R., Gimeno, L., Taboada, J., and Ralph, F. M.: European West Coast atmospheric rivers: A scale to characterize strength and impacts, Weather and Climate Extremes, 31, 100 305, https://doi.org/10.1016/j.wace.2021.100305, 2021.

Fearon, M. G., Doyle, J. D., Ryglicki, D. R., Finocchio, P. M., and Sprenger, M.: The Role of Cyclones in Moisture Transport into the Arctic, Geophysical Research Letters, 48, https://doi.org/10.1029/2020gl090353, 2021.

George, G., Stevens, B., Bony, S., Pincus, R., Fairall, C., Schulz, H., Kölling, T., Kalen, Q. T., Klingebiel, M., Konow, H., Lundry, A., Prange, M., and Radtke, J.: JOANNE: Joint dropsonde Observations of the Atmosphere in tropical North atlaNtic meso-scale Environments, Earth System Science Data, 13, 5253–5272, https://doi.org/10.5194/essd-13-5253-2021, 2021.

Gimeno, L., Nieto, R., VÃ¡zquez, M., and Lavers, D. A.: Atmospheric rivers: a mini-review, Frontiers in Earth Science 2, 2, https://doi.org/10.3389/feart.2014.00002, 2014.

Gorodetskaya, I. V., Tsukernik, M., Claes, K., Ralph, M. F., Neff, W. D., and Lipzig, N. P. M. V.: The role of atmospheric rivers in anomalous snow accumulation in East Antarctica, 41, 6199–6206, https://doi.org/10.1002/2014gl060881, 2014.

Graham, R. M., Cohen, L., Ritzhaupt, N., Segger, B., Graversen, R. G., Rinke, A., Walden, V. P., Granskog, M. A., and Hudson, S. R.: Evaluation of Six Atmospheric Reanalyses over Arctic Sea Ice from Winter to Early Summer, Journal of Climate, 32, 4121–4143, https://doi.org/10.1175/jcli-d-18-0643.1, 2019.

Guan, B.: Tracking Atmospheric Rivers Globally as Elongated Targets (tARget), Version 3 [Dataset], https://doi.org/10.25346/S6/YO15ON, 2022.

Guan, B. and Waliser, D. E.: Detection of atmospheric rivers: Evaluation and application of an algorithm for global studies, Journal of Geophysical Research: Atmospheres, 120, 12 514–12 535, https://doi.org/10.1002/2015jd024257, 2015.

Guan, B. and Waliser, D. E.: Atmospheric rivers in 20 year weather and climate simulations: A multimodel, global evaluation, Journal of Geophysical Research: Atmospheres, 122, 5556–5581, https://doi.org/10.1002/2016jd026174, 2017.

Guan, B. and Waliser, D. E.: Tracking Atmospheric Rivers Globally: Spatial Distributions and Temporal Evolution of Life Cycle Characteristics, Journal of Geophysical Research: Atmospheres, 124, 12 523–12 552, https://doi.org/10.1029/2019jd031205, 2019.

Guan, B., Waliser, D. E., and Ralph, F. M.: An Intercomparison between Reanalysis and Dropsonde Observations of the Total Water Vapor Transport in Individual Atmospheric Rivers, Journal of Hydrometeorology, 19, 321–337, https://doi.org/10.1175/jhm-d-17-0114.1, 2018.

Guan, B., Waliser, D. E., and Ralph, F. M.: A multimodel evaluation of the water vapor budget in atmospheric rivers, Annals of the New York Academy of Sciences, 1472, 139–154, https://doi.org/10.1111/nyas.14368, 2020.

Guan, B., Waliser, D. E., and Ralph, F. M.: Global Application of the Atmospheric River Scale, Journal of Geophysical Research: Atmospheres, 128, https://doi.org/10.1029/2022jd037180, 2023.

Hersbach, H., Bell, B., Berrisford, P., Biavati, G., Horanyi, A., Sabater, J. M., Nicolas, J., Peubey, C., Radu, R., Rozum, I., Schepers, D., Simmons, A., Soci, C., Dee, D., and Thepaut, J.-N.: ERA5 hourly data on pressure levels from 1940 to present, Copernicus Climate Change Service (C3S) Climate Data Store (CDS) [data set] (accessed 22-Apr-2022), https://doi.org/10.24381/cds.bd0915c6, 2018.

Hersbach, H., Bell, B., Berrisford, P., Hirahara, S., Nicolas, J., Peubey, C., Radu, R., Schepers, D., Simmons, A., Soci, C., Abdalla, S., Abellan, X., Balsamo, G., Bechtold, P., Biavati, G., Bidlot, J., Bonavita, M., Chiara, G., Dahlgren, P., Dee, D., Diamantakis, M., Dragani, R., Flemming, J., Forbes, R., Fuentes, M., Geer, A., Haimberger, L., Healy, S., Hogan, R. J., Keeley, S., Laloyaux, P., Lopez, P., Lupu, C., Radnoti, G., Rosnay, P., Rozum, I., Vamborg, F., and Villaume, S.: The ERA5 global reanalysis, Quarterly Journal of the Royal Meteorological Society, 146, 1999–2049, https://doi.org/10.1002/qj.3803, 2020.

Kirbus, B., Tiedeck, S., Camplani, A., Chylik, J., Crewell, S., Dahlke, S., Ebell, K., Gorodetskaya, I., Griesche, H., Handorf, D., Höschel, I., Lauer, M., Neggers, R., Rückert, J., Shupe, M. D., Spreen, G., Walbröl, A., Wendisch, M., and Rinke, A.: Surface impacts and associated mechanisms of a moisture intrusion into the Arctic observed in mid-April 2020 during MOSAiC, Frontiers in Earth Science, 11, https://doi.org/10.3389/feart.2023.1147848, 2023.

Køltzow, M., Schyberg, H., Støylen, E., and Yang, X.: Value of the Copernicus Arctic Regional Reanalysis (CARRA) in representing near-surface temperature and wind speed in the north-east European Arctic, Polar Research, 41, https://doi.org/10.33265/polar.v41.8002, 2022.

Komatsu, K. K., Alexeev, V. A., Repina, I. A., and Tachibana, Y.: Poleward upgliding Siberian atmospheric rivers over sea ice heat up Arctic upper air, Scientific Reports, 8, https://doi.org/10.1038/s41598-018-21159-6, 2018.

Konow, H., Jacob, M., Ament, F., Crewell, S., Ewald, F., Hagen, M., Hirsch, L., Jansen, F., Mech, M., and Stevens, B.: A unified data set of airborne cloud remote sensing using the HALO Microwave Package (HAMP), Earth System Science Data, 11, 921–934, https://doi.org/10.5194/essd-11-921-2019, 2019.

Konow, H., Ewald, F., George, G., Jacob, M., Klingebiel, M., Kölling, T., Luebke, A. E., Mieslinger, T., Pörtge, V., Radtke, J., Schäfer, M., Schulz, H., Vogel, R., Wirth, M., Bony, S., Crewell, S., Ehrlich, A., Forster, L., Giez, A., Gödde, F., Groß, S., Gutleben, M., Hagen, M., Hirsch, L., Jansen, F., Lang, T., Mayer, B., Mech, M., Prange, M., Schnitt, S., Vial, J., Walbröl, A., Wendisch, M., Wolf, K., Zinner, T., Zöger, M., Ament, F., and Stevens, B.: EUREC4A's HALO, Earth System Science Data, 13, 5545–5563, https://doi.org/10.5194/essd-13-5545-2021, 2021.

Lauer, M., Mech, M., and Guan, B.: Global Atmospheric Rivers catalog for ERA5 reanalysis, https://doi.org/10.1594/PANGAEA.957161, 2023a.

Lauer, M., Rinke, A., Gorodetskaya, I., Sprenger, M., Mech, M., and Crewell, S.: Influence of atmospheric rivers and associated weather systems on precipitation in the Arctic, Atmospheric Chemistry and Physics, 23, 8705–8726, https://doi.org/10.5194/acp-23-8705-2023, 2023b.

Lavers, D. A., Pappenberger, F., Richardson, D. S., and Zsoter, E.: ECMWF Extreme Forecast Index for water vapor transport: A forecast tool for atmospheric rivers and extreme precipitation, Geophysical Research Letters, 43, https://doi.org/10.1002/2016gl071320, 2016.

Lenschow, D. H., Savic-Jovcic, V., and Stevens, B.: Divergence and Vorticity from Aircraft Air Motion Measurements, Journal of Atmospheric and Oceanic Technology, 24, 2062–2072, https://doi.org/10.1175/2007jtecha940.1, 2007.

Mattingly, K. S., Mote, T. L., and Fettweis, X.: Atmospheric River Impacts on Greenland Ice Sheet Surface Mass Balance, JGR Atmospheres, 123, 8538–8560, https://doi.org/10.1029/2018jd028714, 2018.

Mech, M., Orlandi, E., Crewell, S., Ament, F., Hirsch, L., Hagen, M., Peters, G., and Stevens, B.: HAMP – the microwave package on the High Altitude and LOng range research aircraft (HALO), Atmospheric Measurement Techniques, 7, 4539–4553, https://doi.org/10.5194/amt-7-4539-2014, 2014.

Nash, D., Waliser, D., Guan, B., Ye, H., and Ralph, F. M.: The Role of Atmospheric Rivers in Extratropical and Polar Hydroclimate, Journal of Geophysical Research: Atmospheres, 123, 6804–6821, https://doi.org/10.1029/2017jd028130, 2018.

Neff, W.: Atmospheric rivers melt Greenland, 8, 857–858, https://doi.org/10.1038/s41558-018-0297-4, 2018.

Neff, W., Compo, G. P., Ralph, F. M., and Shupe, M. D.: Continental heat anomalies and the extreme melting of the Greenland ice surface in 2012 and 1889, Journal of Geophysical Research: Atmospheres, 119, 6520–6536, https://doi.org/10.1002/2014jd021470, 2014.

Neiman, P. J., Wick, G. A., Moore, B. J., Ralph, F. M., Spackman, J. R., and Ward, B.: An Airborne Study of an Atmospheric River over the Subtropical Pacific during WISPAR: Dropsonde Budget-Box Diagnostics and Precipitation Impacts in Hawaii, Monthly Weather Review, 142, 3199–3223, https://doi.org/10.1175/mwr-d-13-00383.1, 2014.

Norris, J. R., Ralph, F. M., Demirdjian, R., Cannon, F., Blomquist, B., Fairall, C. W., Spackman, J. R., Tanelli, S., and Waliser, D. E.: The Observed Water Vapor Budget in an Atmospheric River over the Northeast Pacific, Journal of Hydrometeorology, 21, 2655–2673, https://doi.org/10.1175/jhm-d-20-0048.1, 2020.

Nygård, T., Naakka, T., and Vihma, T.: Horizontal Moisture Transport Dominates the Regional Moistening Patterns in the Arctic, Journal of Climate, 33, 6793–6807, https://doi.org/10.1175/jcli-d-19-0891.1, 2020.

O'Brien, T. A., Wehner, M. F., Payne, A. E., Shields, C. A., Rutz, J. J., Leung, L.-R., Ralph, F. M., Collow, A., Gorodetskaya, I., Guan, B., Lora, J. M., McClenny, E., Nardi, K. M., Ramos, A. M., Tomé, R., Sarangi, C., Shearer, E. J., Ullrich, P. A., Zarzycki, C., Loring, B., Huang, H., Inda-Díaz, H. A., Rhoades, A. M., and Zhou, Y.: Increases in Future AR Count and Size: Overview of the ARTMIP Tier 2 CMIP5/6 Experiment, Journal of Geophysical Research: Atmospheres, 127, https://doi.org/10.1029/2021jd036013, 2022.

Papritz, L. and Dunn-Sigouin, E.: What Configuration of the Atmospheric Circulation Drives Extreme Net and Total Moisture Transport Into the Arctic, Geophysical Research Letters, 47, https://doi.org/10.1029/2020gl089769, 2020.

Papritz, L., Aemisegger, F., and Wernli, H.: Sources and Transport Pathways of Precipitating Waters in Cold-Season Deep North Atlantic Cyclones, Journal of the Atmospheric Sciences, 78, 3349–3368, https://doi.org/10.1175/jas-d-21-0105.1, 2021.

Ralph, F. M., Neiman, P. J., and Wick, G. A.: Satellite and CALJET Aircraft Observations of Atmospheric Rivers over the Eastern North Pacific Ocean during the Winter of 1997/98, Monthly Weather Review, 132, 1721–1745, https://doi.org/10.1175/1520-0493(2004)132<1721:sacaoo>2.0.co;2, 2004.

Ralph, F. M., Neiman, P. J., and Rotunno, R.: Dropsonde Observations in Low-Level Jets over the Northeastern Pacific Ocean from CALJET-1998 and PACJET-2001: Mean Vertical-Profile and Atmospheric-River Characteristics, 133, 889–910, https://doi.org/10.1175/mwr2896.1, 2005.

Ralph, F. M., Iacobellis, S. F., Neiman, P. J., Cordeira, J. M., Spackman, J. R., Waliser, D. E., Wick, G. A., White, A. B., and Fairall, C.: Dropsonde Observations of Total Integrated Water Vapor Transport within North Pacific Atmospheric Rivers, Journal of Hydrometeorology, 18, 2577–2596, https://doi.org/10.1175/jhm-d-17-0036.1, 2017.

Ralph, F. M., Rutz, J. J., Cordeira, J. M., Dettinger, M., Anderson, M., Reynolds, D., Schick, L. J., and Smallcomb, C.: A Scale to Characterize the Strength and Impacts of Atmospheric Rivers, Bulletin of the American Meteorological Society, 100, 269–289, https://doi.org/10.1175/bams-d-18-0023.1, 2019.

Rostosky, P. and Spreen, G.: Relevance of warm air intrusions for Arctic satellite sea ice concentration time series, The Cryosphere, 17, 3867–3881, https://doi.org/10.5194/tc-17-3867-2023, 2023.

Schyberg, H., Yang, X., Koltzow, M., Amstrup, B., Bakketun, A., Bazile, E., Bojarova, J., Box, J. E., Dahlgren, P., Hagelin, S., Homleid, M., Horanyi, A., Hoyer, J., Johansson, A., Killie, M., Koernich, H., Moigne, P. L., Lindskog, M., Manninen, T., Englyst, P. N., Nielsen, K., Olsson, E., Palmason, B., Aros, C. P., Randriamampianina, R., Samuelsson, P., Stappers, R., Stoylen, E., Thorsteinsson, S., Valkonen, T., and Wang, Z.: Arctic regional reanalysis on pressure levels from 1991 to present, Copernicus Climate Change Service (C3S) Climate Data Store(CDS) (accessed on 16-Jun-2022), https://doi.org/10.24381/CDS.E3C841AD, 2021.

Seager, R. and Henderson, N.: Diagnostic Computation of Moisture Budgets in the ERA-Interim Reanalysis with Reference to Analysis of CMIP-Archived Atmospheric Model Data, Journal of Climate, 26, 7876–7901, https://doi.org/10.1175/jcli-d-13-00018.1, 2013.

Shupe, M. D., Rex, M., Blomquist, B., Persson, P. O. G., Schmale, J., Uttal, T., Althausen, D., Angot, H., Archer, S., Bariteau, L., Beck, I., Bilberry, J., Bucci, S., Buck, C., Boyer, M., Brasseur, Z., Brooks, I. M., Calmer, R., Cassano, J., Castro, V., Chu, D., Costa, D., Cox, C. J., Creamean, J., Crewell, S., Dahlke, S., Damm, E., de Boer, G., Deckelmann, H., Dethloff, K., Dütsch, M., Ebell, K., Ehrlich, A., Ellis, J., Engelmann, R., Fong, A. A., Frey, M. M., Gallagher, M. R., Ganzeveld, L., Gradinger, R., Graeser, J., Greenamyer, V., Griesche, H., Griffiths, S., Hamilton, J., Heinemann, G., Helmig, D., Herber, A., Heuzé, C., Hofer, J., Houchens, T., Howard, D., Inoue, J., Jacobi, H.-W., Jaiser, R., Jokinen, T., Jourdan, O., Jozef, G., King, W., Kirchgaessner, A., Klingebiel, M., Krassovski, M., Krumpen, T., Lampert, A., Landing, W., Laurila, T., Lawrence, D., Lonardi, M., Loose, B., Lüpkes, C., Maahn, M., Macke, A., Maslowski, W., Marsay, C., Maturilli,

M., Mech, M., Morris, S., Moser, M., Nicolaus, M., Ortega, P., Osborn, J., Pätzold, F., Perovich, D. K., Petäjä, T., Pilz, C., Pirazzini, R., Posman, K., Powers, H., Pratt, K. A., Preußer, A., Quéléver, L., Radenz, M., Rabe, B., Rinke, A., Sachs, T., Schulz, A., Siebert, H., Silva, T., Solomon, A., Sommerfeld, A., Spreen, G., Stephens, M., Stohl, A., Svensson, G., Uin, J., Viegas, J., Voigt, C., von der Gathen, P., Wehner, B., Welker, J. M., Wendisch, M., Werner, M., Xie, Z., and Yue, F.: Overview of the MOSAiC expedition: Atmosphere, Elementa: Science of the Anthropocene, 10, https://doi.org/10.1525/elementa.2021.00060, 2022.

Skamarock, W. C., Park, S.-H., Klemp, J. B., and Snyder, C.: Atmospheric Kinetic Energy Spectra from Global High-Resolution Nonhydrostatic Simulations, Journal of the Atmospheric Sciences, 71, 4369–4381, https://doi.org/10.1175/jas-d-14-0114.1, 2014.

Stevens, B., Ament, F., Bony, S., Crewell, S., Ewald, F., Gross, S., Hansen, A., Hirsch, L., Jacob, M., Kölling, T., Konow, H., Mayer, B., Wendisch, M., Wirth, M., Wolf, K., Bakan, S., Bauer-Pfundstein, M., Brueck, M., Delanoë, J., Ehrlich, A., Farrell, D., Forde, M., Gödde, F., Grob, H., Hagen, M., Jäkel, E., Jansen, F., Klepp, C., Klingebiel, M., Mech, M., Peters, G., Rapp, M., Wing, A. A., and Zinner, T.: A High-Altitude Long-Range Aircraft Configured as a Cloud Observatory: The NARVAL Expeditions, Bulletin of the American Meteorological Society, 100, 1061–1077, https://doi.org/10.1175/bams-d-18-0198.1, 2019.

Tan, Y., Yang, S., Zwiers, F., Wang, Z., and Sun, Q.: Moisture budget analysis of extreme precipitation associated with different types of atmospheric rivers over western North America, Climate Dynamics, 58, 793–809, https://doi.org/10.1007/s00382-021-05933-3, 2021.

Terpstra, A., Gorodetskaya, I. V., and Sodemann, H.: Linking Sub-Tropical Evaporation and Extreme Precipitation Over East Antarctica: An Atmospheric River Case Study, Journal of Geophysical Research: Atmospheres, 126, https://doi.org/10.1029/2020jd033617, 2021.

Vázquez, M., Algarra, I., Eiras-Barca, J., Ramos, A. M., Nieto, R., and Gimeno, L.: Atmospheric Rivers over the Arctic: Lagrangian Characterisation of Their Moisture Sources, Water, 11, 41, https://doi.org/10.3390/w11010041, 2018.

Viceto, C., Gorodetskaya, I. V., Rinke, A., Maturilli, M., Rocha, A., and Crewell, S.: Atmospheric rivers and associated precipitation patterns during the ACLOUD and PASCAL campaigns near Svalbard (May–June 2017): case studies using observations, reanalyses, and a regional climate model, Atmospheric Chemistry and Physics, 22, 441–463, https://doi.org/10.5194/acp-22-441-2022, 2022.

Wendisch, M., Handorf, D., Tegen, I., Neggers, R., and Spreen, G.: Glimpsing the Ins and Outs of the Arctic Atmospheric Cauldron, Eos, 102, https://doi.org/10.1029/2021eo155959, 2021.

Wendisch, M., Brückner, M., Crewell, S., Ehrlich, A., Notholt, J., Lüpkes, C., Macke, A., Burrows, J. P., Rinke, A., Quaas, J., Maturilli, M., Schemann, V., Shupe, M. D., Akansu, E. F., Barrientos-Velasco, C., Bärfuss, K., Blechschmidt, A.-M., Block, K., Bougoudis, I., Bozem, H., Böckmann, C., Bracher, A., Bresson, H., Bretschneider, L., Buschmann, M., Chechin, D. G., Chylik, J., Dahlke, S., Deneke, H., Dethloff, K., Donth, T., Dorn, W., Dupuy, R., Ebell, K., Egerer, U., Engelmann, R., Eppers, O., Gerdes, R., Gierens, R., Gorodetskaya, I. V., Gottschalk, M., Griesche, H., Gryanik, V. M., Handorf, D., Harm-Altstädter, B., Hartmann, J., Hartmann, M., Heinold, B., Herber, A., Herrmann, H., Heygster, G., Höschel, I., Hofmann, Z., Hölemann, J., Hünerbein, A., Jafariserajehlou, S., Jäkel, E., Jacobi, C., Janout, M., Jansen, F., Jourdan, O., Jurányi, Z., Kalesse-Los, H., Kanzow, T., Käthner, R., Kliesch, L. L., Klingebiel, M., Knudsen, E. M., Kovács, T., Körtke, W., Krampe, D., Kretzschmar, J., Kreyling, D., Kulla, B., Kunkel, D., Lampert, A., Lauer, M., Lelli, L., von Lerber, A., Linke, O., Löhnert, U., Lonardi, M., Losa, S. N., Losch, M., Maahn, M., Mech, M., Mei, L., Mertes, S., Metzner, E., Mewes, D., Michaelis, J., Mioche, G., Moser, M., Nakoudi, K., Neggers, R., Neuber, R., Nomokonova, T., Oelker, J., Papakonstantinou-Presvelou, I., Pätzold, F., Pefanis, V., Pohl, C., van Pinxteren, M., Radovan, A., Rhein, M., Rex, M., Richter, A., Risse, N., Ritter, C., Rostosky, P., Rozanov, V. V., Donoso, E. R., Saavedra Garfias, P., Salzmann, M., Schacht, J., Schäfer, M., Schneider, J., Schnierstein, N., Seifert, P., Seo, S., Siebert, H., Soppa, M. A., Spreen, G., Stachlewska, I. S., Stapf, J., Stratmann, F., Tegen, I., Viceto, C., Voigt, C., Vountas, M., Walbröl, A., Walter, M., Wehner, B., Wex, H., Willmes, S., Zanatta, M., and Zeppenfeld, S.: Atmospheric and Surface Processes, and Feedback Mechanisms

Determining Arctic Amplification: A Review of First Results and Prospects of the (AC)3 Project, Bulletin of the American Meteorological Society, 104, E208–E242, https://doi.org/10.1175/bams-d-21-0218.1, 2023.

Wong, S., Genio, A. D. D., Wang, T., Kahn, B. H., Fetzer, E. J., and L'Ecuyer, T. S.: Responses of Tropical Ocean Clouds and Precipitation to the Large-Scale Circulation: Atmospheric-Water-Budget-Related Phase Space and Dynamical Regimes, Journal of Climate, 29, 7127–7143, https://doi.org/10.1175/jcli-d-15-0712.1, 2016.

Woods, C. and Caballero, R.: The Role of Moist Intrusions in Winter Arctic Warming and Sea Ice Decline, Journal of Climate, 29, 4473–4485, https://doi.org/10.1175/jcli-d-15-0773.1, 2016.

You, C., Tjernström, M., and Devasthale, A.: Warm and moist air intrusions into the winter Arctic: a Lagrangian view on the near-surface energy budgets, Atmospheric Chemistry and Physics, 22, 8037–8057, https://doi.org/10.5194/acp-22-8037-2022, 2022.

Zavadoff, B. L. and Kirtman, B. P.: North Atlantic Summertime Anticyclonic Rossby Wave Breaking: Climatology, Impacts, and Connections to the Pacific Decadal Oscillation, Journal of Climate, 32, 485–500, https://doi.org/10.1175/jcli-d-18-0304.1, 2018.

Zhang, C., Tung, W.-W., and Cleveland, W. S.: Atlas of Arctic Atmospheric River Climatology Based on ERA5 and MERRA-2, https://doi.org/10.1002/essoar.10511981.1, 2022.

Zheng, M., Monache, L. D., Wu, X., Ralph, F. M., Cornuelle, B., Tallapragada, V., Haase, J. S., Wilson, A. M., Mazloff, M., Subramanian, A., and Cannon, F.: Data Gaps within Atmospheric Rivers over the Northeastern Pacific, Bulletin of the American Meteorological Society, 102, E492–E524, https://doi.org/10.1175/bams-d-19-0287.1, 2021.